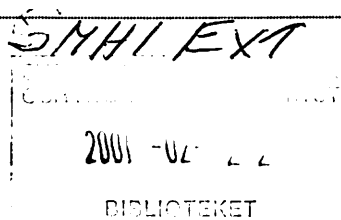


BALTEX Radar Data Centre Products and their Methodologies

Cover: Subimage of a twelve-hour accumulated precipitation product (RR) from July 19, 2000, at 18 UTC, the rains from which triggered severe floods in central Sweden.



RMK
No. 90, Aug 2000

BALTEX Radar Data Centre Products and their Methodologies

**Daniel B. Michelson, Swedish Meteorological and Hydrological
Institute**

**Tage Andersson, Swedish Meteorological and Hydrological
Institute**

Jarmo Koistinen, Finnish Meteorological Institute

**Christopher G. Collier, Telford Institute of Environmental Systems,
University of Salford**

Johann Riedl, German Weather Service

Jan Szturc, Institute of Meteorology and Water Management

Uta Gjertsen, The Norwegian Meteorological Institute

Aage Nielsen, Danish Meteorological Institute

Søren Overgaard, Danish Meteorological Institute

Report Summary / Rapportsammanfattning

Issuing Agency/Utgivare		Report number/Publikation	
Swedish Meteorological and Hydrological Institute SE-601 76 NORRKÖPING Sweden		RMK No. 90	
		Report date/Utgivningsdatum	
		August 2000	
Author (s)/Författare			
Daniel B. Michelson, Tage Andersson, Jarmo Koistinen, Christopher G. Collier, Johann Riedl, Jan Szturc, Uta Gjertsen, Aage Nielsen, and Søren Overgaard			
Title (and Subtitle)/Titel			
BALTEX Radar Data Centre Products and their Methodologies			
Abstract/Sammandrag			
<p>The Baltic Sea Experiment (BALTEX) is the European regional project within the Global Energy and Water Cycle Experiment (GEWEX). The BALTEX Working Group on Radar (WGR) is responsible for coordinating weather radar activities within the framework of BALTEX, including the establishment and operation of a Radar Data Centre (BRDC) which can provide BALTEX with wind and precipitation datasets. This report presents the state of the WGR and the BALTEX Radar Network (BALTRAD). Those products being generated at the BRDC are presented and discussed, as are the methods used to create them.</p> <p>The BALTRAD network consists of 29, mostly C-band, radars in six countries. Communications to/from the BRDC are conducted both through operational lines and through provisional Internet-based solutions. The BRDC operates in near-real time. Individual radar images containing radar reflectivity factor (dBZ) are produced with a temporal resolution of 15 min. These are combined to create composite images, also every 15 minutes. A systematic gauge correction method is introduced for application to point observations from the synoptical network. These corrected gauge observations are used together with radar sums to create spatially continuous, gauge-adjusted three- and twelve-hour accumulations. The gauge adjustment technique is shown to minimize the bias between radar and gauge observations, while also reducing the range dependency on the radar data. All image products have horizontal resolutions of 2 km. A wind profile product is also created using VAD and VVP techniques.</p>			
Key words/sök-, nyckelord			
Weather radar, Baltic Sea Experiment, BALTEX, radar network, radar imagery, composite imagery, gauge correction, gauge adjustment, accumulated precipitation, wind profiles, datasets			
Supplementary notes/Tillägg		Number of pages/Antal sidor	Language/Språk
		76	English
ISSN and title/ISSN och titel			
0347-2116 SMHI Reports Meteorology Climatology			
Report available from/Rapporten kan köpas från:			
SMHI SE-601 76 NORRKÖPING Sweden			

Contents

Contents	i
1 Introduction	1
1.1 Objectives	2
2 The BALTEX Working Group on Radar and the BALTRAD Network	4
2.1 BALTEX WGR	4
2.2 Norway	4
2.3 Finland	5
2.4 Sweden	5
2.5 Denmark	6
2.6 Germany	6
2.7 Poland	7
2.8 Baltic States and Russia	7
2.9 Network communications	11
3 Radar Reflectivity Factor Images (DBZ)	12
3.1 Cartographic projections	12
3.2 Cartesian representations of radar data	13
3.3 Speckle reduction	15
3.4 DNMI	15
3.5 FMI	16
3.6 SWERAD	16
3.7 DMI	17
3.8 DWD	19
3.9 IMGW	21
4 Composite Images of Radar Reflectivity Factor (DBZC)	22
4.1 Area definition	22
4.2 Compositing algorithms	22
4.2.1 Radar beam refraction	23
4.2.2 Distance to the surface	24
4.3 DBZC compositing algorithm	25
4.4 Quality control	26
4.4.1 Method performance and limitations	29
5 Systematic Correction of Gauge Observations	32
5.1 Gauge types in the BALTEX Region	34
5.2 Dynamic Correction Model	34
5.3 Input variables	35
5.4 Sensitivities of the correction equations	37
6 Accumulated Precipitation (RR)	41
6.1 Temporal integration periods	41
6.2 Area definitions	41
6.3 Gauge radar adjustment background	41

6.4	Accumulated precipitation from radar	43
6.4.1	Three hour sums	43
6.4.2	Twelve hour sums	44
6.5	G/R point pairs and their relationship with distance	44
6.6	Spatial adjustment factor field	47
6.7	Radar normalization through preliminary adjustment	48
6.8	Example case	51
6.9	Three hourly adjustment	53
6.10	Treatment of areas without radar coverage	53
6.11	Validation	58
7	Vertical Wind and Reflectivity Profiles (WP)	60
7.1	DNMI	60
7.2	SMHI	61
7.3	FMI	63
7.4	Example	66
8	Summary	68
9	Acknowledgements	70
10	List of Acronyms	71
11	References	73

1 Introduction

Accurate precipitation measurements are essential to improve scientific understanding, and to develop forecasting systems to both warn of hazards and enable the optimisation of management procedures. The role of precipitating clouds in climate is fundamental in studies of climate change at the global, regional and local scale. Rain is a key component of the hydrological cycle yet is poorly observed in many areas, particularly over the oceans and large sea areas such as the Baltic (Browning 1990).

Meso-scale weather systems, which result in most of the weather manifestation affecting human activities, are forced either by the large-scale flow or by the lower boundary. Thus, it is necessary that this forcing should be correctly specified if a good weather forecast is to be obtained. The primary response of the atmosphere to forcing occurs through condensation of water, and the consequent release of latent heat. Hence a detailed specification of the three-dimensional moisture distribution is required for the accurate prediction of the meso-scale response to forcing. In particular, the three-dimensional specification of rainfall enables latent heating to be input to numerical models, thus providing a modification of the initial state variables. The result may have a significant impact upon future forecasts, and therefore must be understood in some detail. Precipitation data, at much increased spatial and temporal resolution, are therefore needed as an essential element of model initialisation procedures, and to verify numerical model studies of meteorological systems and climatic dynamics.

Unfortunately, small errors in the observations used to make weather forecasts can cause large errors in the forecasts themselves (Stensrud and Fritsch 1994). Sometimes quite complex feedback mechanisms between precipitation, soil moisture and surface fluxes lead to unexpected outcomes. The water budget of the Baltic Sea remains uncertain and its determination is limited to analysis and modelling activities where coastal weather station data are extrapolated out over the Baltic (Rubel 1998; Omstedt et al. 1997; Rubel 1996). Indeed, it is not clear whether net precipitation (precipitation minus evaporation) is positive or negative over the sea area. Detailed spatial and temporal measurements of precipitation and other meteorological variables are needed to clarify these uncertainties (Rutgersson et al. 2000).

Precipitation is the primary input to hydrological forecasting procedures. A wide range of numerical models has been developed to relate continuous measurements of net precipitation to river flow. Some models make use of river catchment integrated precipitation, whereas others require such information over small areas within individual river subcatchments (Collier 1996). Whilst the accuracy with which precipitation measurements are needed is very important, it needs to be specified with a knowledge of the hydrological characteristics of the river catchment being modelled. Reproducibility in space, time and quantitative accuracy is very important since consistent error characteristics are the basis of sound model calibration. Without wide area measurements of precipitation, river flow cannot be predicted with any certainty. Clearly accurate precipitation estimates over lakes and the Baltic Sea are essential if the whole Baltic basin is to be modelled successfully (Graham 2000).

BALTEX, the Baltic Sea Experiment, has been established during recent years, as one out of five continental scale experiments within the Global Energy and Water Cycle Experiment (GEWEX), which is guided and permanently monitored by the World Climate Research Programme (WCRP). The general aim of the BALTEX is to investigate the energy and water budgets within the Baltic Sea water catchment area and their dependencies on external forcing by the global atmospheric and oceanic circulation, to develop coupled comprehensive models including the atmosphere, the land surface with vertical and horizontal hydrological processes, the Baltic Sea and the ice. The general objectives include also development of transportable methodologies for such studies over other larger river drainage basins on the globe.

The details of the BALTEX programme are described in the Initial Implementation Plan (BALTEX 1995). The BALTEX strategy makes intensive use of available ground- and satellite-based information and of modelling capabilities which have been developed in several of the participating countries. The consistent use of weather radar to achieve the objectives of BALTEX is clearly defined (Brandt et al. 1996) and is the responsibility of the BALTEX Working Group on Radar (WGR). In the frame of GEWEX and BALTEX the improvement of precipitation analysis through a dedicated BALTEX Radar Network (BALTRAD) will be beneficial also for medium and long-term climate prediction, climate impact studies, improvement of observational techniques and networks design, as well as environmental aspects.

Satellite remote sensing techniques alone cannot provide reliable precipitation observations at high latitudes. Rain gauges are almost unavailable over the sea. Weather radars are the only sensors which are able to provide precipitation observations, with high spatial and temporal resolution, simultaneously over both land and sea. The activities of the BALTEX WGR have lead to the establishment and operation of the BALTEX Radar Data Centre (BRDC) at the Swedish Meteorological and Hydrological Institute (SMHI). The BRDC is designed to collect data from those radars in and proximate to the Baltic Sea and it's drainage basin (BALTRAD), to process these data into series of homogeneous products, to disseminate these products to BALTEX data users, and to archive all data and products. These activities are a major contribution to the BALTEX Main Experiment, called BRIDGE, with its Base-Line Period taking place from October 1, 1999 to February 28, 2002.

1.1 Objectives

The objectives of this report are summarized in the following points.

- to briefly present the BALTEX WGR,
- to present the current state of the BALTRAD network and those institutes providing data to the BRDC,
- to present those products comprising the datasets generated for BRIDGE, and

- to present and discuss those methods being used to generate the BRDC products.

The focus of this report is to document the state of the weather radar activities in BALTEX. The methods presented in Chapters 3-7 are done so without elaborated reviews of the state of the art within each area of research. The use of references to the literature is thus deliberately conservative.

The report is targeted towards users of BRDC products. While the use of jargon specific to the research field is inevitable, an effort has been made to present some of the fundamental characteristics of radars and radar data to new users such that they may find it easier to start working with the products.

A number of areas requiring future research are also outlined.

2 The BALTEX Working Group on Radar and the BALTRAD Network

2.1 BALTEX WGR

The BALTEX WGR was established by the BALTEX Scientific Steering Group as a part of the experiment's infrastructure, and its terms of reference are presented in BALTEX (1995). The operative objectives of the WGR do not differ significantly from the terms of reference and can be summarized in the following points.

- to promote the use of weather radar as a prime wind and precipitation observation system within the framework of BALTEX,
- to coordinate the use of weather radar in BALTEX,
- to encourage the establishment of a Radar Data Centre for use during the BALTEX Main Experiment (BRIDGE),
- to define those radar-based products to be generated and archived at the BRDC, and distributed to BALTEX Data Users,
- to conduct research and development on improving the quality and quantitative use of those radar-based products generated at the BRDC,
- to meet regularly and keep updated on the status of weather radar in the BALTEX Region, and
- to inform the research community of its activities.

The activities carried out by the BALTEX Working Group on Radar (WGR) have resulted in a radar network which operates in near-real time under the umbrella of BALTEX. This is the BALTRAD network, previously presented and described by Koistinen and Michelson (1997) and Michelson et al. (1999). The characteristics of these radars, and the institutes operating them, are updated from these previous works in the following sections. The information is summarized in Figures 2.1-2.2 and in Table 2.1. The following sections present those institutes and radars which contribute to BALTRAD and the BRDC.

2.2 Norway

The Norwegian Meteorological Institute (DNMI) operates the national network of weather radars. This network presently consists of two nodes: Oslo and Hægebostad, located outside the capital city and on the south coast, respectively. Radar Hægebostad has been operational since the beginning of May, 2000. Both radars operate at C-band (5.6 GHz) and both have Doppler capability.

The manufacturer of Radar Oslo is Ericsson. This radar operates both in non-Doppler and Doppler modes. The maximum operational ranges these modes is 240 and 120 km, respectively. Data from this radar are made available within NORDRAD (Nordic Weather Radar System) in the radar's Gnomonic projection. The software used on this radar is Ericsson's EWIS system.

Radar Hægebostad is manufactured by Gematronik and was installed during the second half of 1999. It is the first such radar to be delivered with a digital receiver. Doppler capability is enabled to a maximum operational range of 240-250 *km*. Gematronik's RAVIS software operates this radar and its Rainbow software generates its products.

DNMI has planned an expansion of the national network and more nodes may appear during the course of BALTEX.

2.3 Finland

The Finnish Meteorological Institute (FMI) operates the national network of weather radars, which currently consists of seven nodes. Of these nodes, one, Radar Rovaniemi, consists of a Russian MRL-5 non-Doppler radar operating at X-band. The software running this radar is Ericsson EWIS.

The other six radars all operate at C-band and are made by Gematronik. The antenna controllers, signal processors and software systems are, however, made by Sigmat Inc. The Sigmat RVP6 is the signal processor and the IRIS software runs the radars. All these radars have Doppler capability to a maximum operational range of 250 *km*.

Data from these radars are made available in each radar's Gnomonic projection.

Radar Rovaniemi is in the process of being replaced by a new Gematronik radar. The location will be slightly different and the new site designation is Luosto. A Sigmat RVP7 digital receiver and signal processor will operate on this new radar, which is scheduled to be operational during 2000.

2.4 Sweden

The Swedish Meteorological and Hydrological Institute (SMHI) and the Swedish Air Force jointly operate the Swedish weather radar network (SWERAD). These radars are all manufactured by Ericsson, they all operate at C-band, and they all have Doppler capability. Their characteristics are similar to those given for Radar Oslo in Section 2.2, with the clarification that the radar at Stockholm-Arlanda is one of the earliest Ericsson radars and contains a slightly different configuration.

The SWERAD nodes may undertake a "reshuffling" during BALTEX. Starting during 2000, a new node (also an Ericsson) may appear near the town of Ängelholm, in

the southwest roughly at the same latitude as Radar Karlskrona. Once this has taken place, Radar Göteborg may be moved to a more inland site and Radar Norrköping may be moved to the north to cover the gap in national coverage between Radars Östersund and Kiruna. Alternatively, a new or other used radar may be installed in the north. These plans are not yet definite and may be subject to change.

2.5 Denmark

The Danish Meteorological Institute (DMI) operates a national network consisting of three Ericsson, C-band radars. Radar Copenhagen is the same generation as Swedish Radar Arlanda and does not have Doppler capability. The other two nodes have Doppler and characteristics similar to those given for Radar Oslo in Section 2.2.

Data from Radars Copenhagen and Sindal are provided through the NORDRAD infrastructure although they are not actually part of the NORDRAD network. Data from Rømø are provided through the Internet.

DMI also has plans to reshuffle their radars. A new node is planned for Holbæk, Sealand. Once this has taken place, Radar Copenhagen may be moved to the island of Bornholm. Again, these plans are not yet definite and may be subject to change.

2.6 Germany

The German Weather Service (DWD) operates a national network consisting of a mix of radars from different manufacturers which operate at C-band. For the purposes of BALTEX and the BRDC, data from four of these radars are used: Hamburg-Fuhlsbüttel, Rostock, Berlin-Tempelhof, and Dresden.

Radars Hamburg and Berlin are both made by Enterprise Electronics Corp. (EEC). Radar Hamburg does not have Doppler capability, whereas Berlin was dopplerized in 1999 with a Sigmet RVP7 digital receiver and signal processor. Radar Rostock is made by Gematronik and contains a Sigmet RVP6 signal processor, much like the current Finnish radars. However, all of these radars run RMV software developed by the DWD. Maximum operational range is 230 km. Radar Dresden was installed and configured during the second half of 1999; it is again a Gematronik radar with a Sigmet RVP6 signal processor.

Data exchange between the DWD and BRDC takes place through the ETR lines presented and described below in Section 2.9. Products received at the BRDC have a horizontal resolution of 2 km.

2.7 Poland

The Institute of Meteorology and Water Management (IMGW) operates the national network of two radars, located in Legionowo, outside Warsaw, and Katowice, near Cracow.

Radar Legionowo is an MRL-5, like FMI's Radar Rovaniemi. It operates operationally at X-band and at a maximum range of 240 km. It does not have Doppler capability. Software developed by the IMGW operates this radar and generates its products. Data received at the BRDC have a horizontal resolution of 4 km and the radar's Gnomonic projection.

Radar Katowice is a new C-band Gematronik radar with Doppler capability. Operational maximum range is 200 km and products' horizontal resolution is 1 km. Data to the BRDC arrives through the Internet.

There are ambitious plans to extend the Polish weather radar network as part of the establishment of a large monitoring, forecasting and protection system (IMGW 1999). These plans involve a network comprising eight radars within the next few years along with enhanced communications infrastructure for domestic and international data exchange. Due to Poland's central position in the BALTEX Region, any developments to this national network are of potential benefit to BALTEX and the BRDC's activities.

2.8 Baltic States and Russia

Radar data from these areas are not presently available on-line for any purposes outside the areas, and thus not for BALTEX either. Radars are either not digitized or current communications infrastructure cannot support such activities. An example of the latter is a network of MRL-5 radars in the St. Petersburg area, the data from which simply cannot be transferred reliably to the BRDC. There are, however, plans which will hopefully improve the situation in this region which may benefit BALTEX.

The Estonian Meteorological and Hydrological Institute (EMHI) has purchased a new Gematronik radar and there are plans to install it in the Tallin area during 2000. EMHI plans on buying and installing one additional radar.

The Latvian Hydrometeorological Agency plans on purchasing a radar system. It remains to be seen when this may take place. The designated radar site is Riga airport. The potential benefit to BALTEX is that radar coverage of the Gulf of Riga may be enabled.

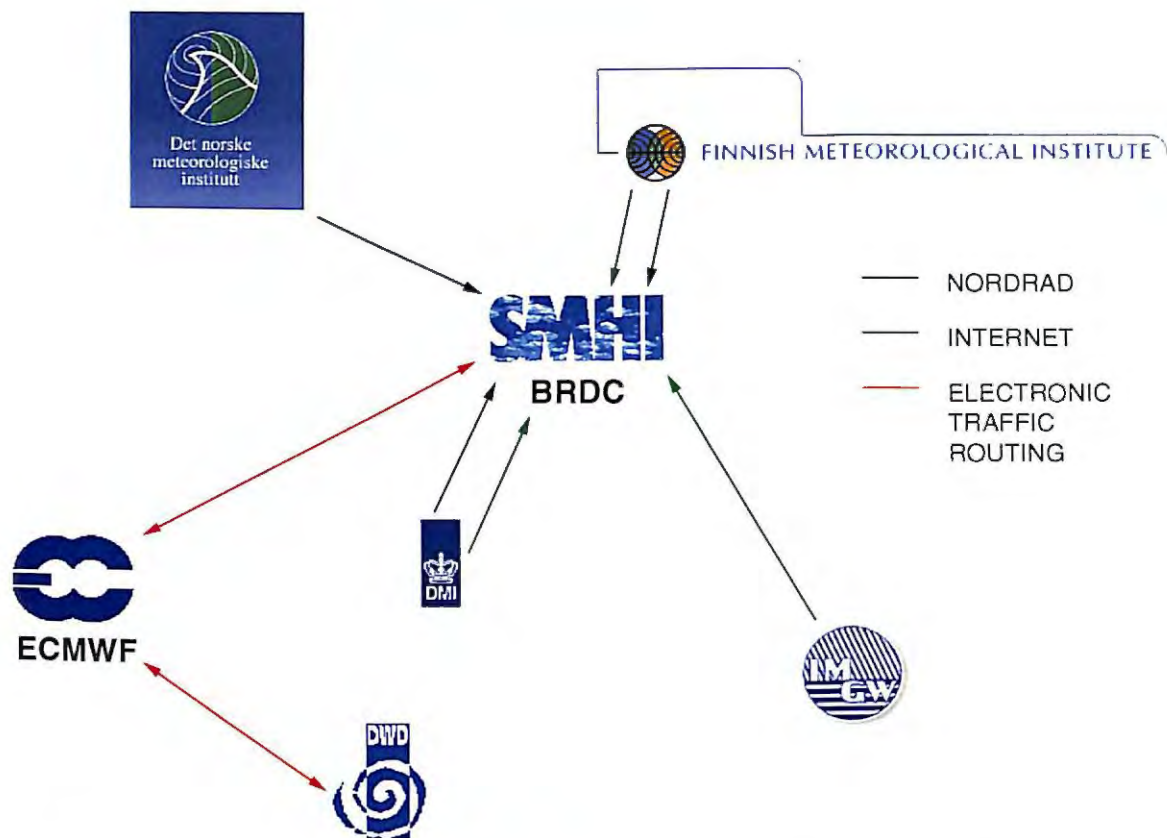


Figure 2.1: Communications to/from the BRDC from contributing institutes.



Figure 2.2: The locations of BALTRAD radars, each with a three letter node designation defined in Table 2.1.

Table 2.1: Summarized characteristics of BALTRAD radars.

Node	Place	Lat.	Lon.	Height (m)	Hardware	Software	Band	Doppler	Operator	Since
Norwegian										
OSL	Oslo	59.858	10.387	458	Ericsson	EWIS	C	Y	DNMI	1992
HGB	Hægebostad	58.355	7.158	631	Gematronik	Rainbow	C	Y	DNMI	1999
Finnish										
KOR	Korpo	60.128	21.646	61	Gematronik	IRIS	C	Y	FMI	1997
VAN	Vantaa	60.271	24.873	83	Gematronik	IRIS	C	Y	FMI	1993
IKA	Ikaalinen	61.767	23.080	154	Gematronik	IRIS	C	Y	FMI	1993
KUO	Kuopio	62.862	27.385	268	Gematronik	IRIS	C	Y	FMI	1995
ANJ	Anjalankoski	60.904	27.111	139	Gematronik	IRIS	C	Y	FMI	1993
UTA	Utajärvi	64.774	26.323	118	Gematronik	IRIS	C	Y	FMI	1997
ROV	Rovaniemi	66.608	25.844	209	MRL5	EWIS	X	N	FMI	1988
Swedish										
KKR	Karlskrona	56.300	15.610	122	Ericsson	EWIS	C	Y	SWERAD	1990
HEM	Hemse	57.240	18.390	56	Ericsson	EWIS	C	Y	SWERAD	1990
GBG	Göteborg	57.720	12.170	164	Ericsson	EWIS	C	Y	SWERAD	1988
NKP	Norrköping	58.617	16.117	57	Ericsson	EWIS	C	Y	SWERAD	1983
ARL	Arlanda	59.660	17.950	75	Ericsson	EWIS	C	Y	SWERAD	1986
LEK	Leksand	60.723	14.880	458	Ericsson	EWIS	C	Y	SWERAD	1994
HUD	Hudiksvall	61.572	16.716	388	Ericsson	EWIS	C	Y	SWERAD	1992
OSU	Östersund	63.175	14.454	465	Ericsson	EWIS	C	Y	SWERAD	1995
OVI	Örnsköldsvik	63.640	18.400	522	Ericsson	EWIS	C	Y	SWERAD	1991
LUL	Luleå	65.550	22.133	35	Ericsson	EWIS	C	Y	SWERAD	1993
KIR	Kiruna	67.710	20.622	646	Ericsson	EWIS	C	Y	SWERAD	1996

continued on next page

continued from previous page

Node	Place	Lat.	Lon.	Height (m)	Hardware	Software	Band	Doppler	Operator	Since
Danish										
SIN	Sindal	57.489	10.136	93	Ericsson	EWIS	C	Y	DMI	1994
CPH	Copenhagen	55.6	12.62	5	Ericsson	EWIS	C	N	DMI	1986
ROM	Rømø	55.173	8.552	10	Ericsson	EWIS	C	Y	DMI	1992
German										
HAM	Hamburg	53.623	9.998	46	EEC	RMV (DWD)	C	N	DWD	1990
ROS	Rostock	54.174	12.059	35	Gematronik	RMV (DWD)	C	Y	DWD	1995
BLN	Berlin	52.479	13.389	80	EEC	RMV (DWD)	C	Y	DWD	1991
DRE	Dresden	51.121	13.765	250	Gematronik	RMV (DWD)	C	Y	DWD	2000
Polish										
LEG	Legionowo	52.4	20.967	125	MRL5	IMGW	XS	N	IMGW	1991
KAT	Katowice	50.142	18.726	357	Gematronik	Rainbow	C	Y	IMGW	1995

2.9 Network communications

The NORDRAD collaboration has been operational since 1993 (Carlsson 1995) and presently manages the exchange of radar products among DNMI, SMHI and FMI. Data products provided within the NORDRAD collaboration have horizontal resolutions of 2 *km* and 1 *km*. This is based on the assumption that non-Doppler data is produced at 2 *km* resolution and Doppler data at 1 *km*. While most products are exchanged in the NORDRAD file format, wind profiles are being exchanged using an unofficial version of the BUFR code being developed within the framework of the Operational Programme for the Exchange of Weather Radar Information (OPERA 1999). The international exchange takes place through permanent lines using the DECnet protocol. Bandwidth varies between 9.6-64 kbit/s. Exchange of data between DMI and SMHI uses these lines and the NORDRAD infrastructure.

The European Centre for Medium Range Weather Forecasting (ECMWF) has a network of permanent lines between it and its member states. Bandwidth varies but is commonly 64 kbit/s. Using TCP/IP based protocols, the ECMWF has developed a system called Electronic Transfer Routing (ETR) with which it is possible to exchange data between member states, relayed through the ECMWF. This ETR service is used for the purposes of data exchange between the DWD and BRDC.

During 2000, some of the operational exchange will be re-routed to the new Regional Meteorological Data Communication Network (RMDCN).

For exchange of data from FMI, IMGW, and data from DMI's Radar Rømo, the regular Internet is used with different solutions; password protected ftp is used, as is the Secure Shell from SSH Communications Security Ltd. The Polish data is transferred manually from the IMGW in Legionowo.

3 Radar Reflectivity Factor Images (DBZ)

The overall objective is to create a set of homogenous products, designated “DBZ”, containing radar reflectivity factor (dBZ) which can be used as a basis for generating higher level products.

Each BALTRAD radar produces scans of data in polar coordinates (elevation angle, azimuth angle and slant range) and these have different configurations depending on a given radar’s hardware, software and operator. A prerequisite for dealing with networked radars is being able to transform these polar data to a common cartesian projection. After a brief description of the projection systems used at the BRDC, and a short introduction to common cartesian representations of radar data, follows a presentation of how radar data from different sources are homogenized at the BRDC.

3.1 Cartographic projections

There are a number of different projection systems being used by those institutes contributing data to the BRDC, and by the BRDC itself. These are shortly presented here. All of the projections are described in detail by Evenden (1995). An appropriate reference on projections is Richardus and Adler (1972).

A Gnomonic projection is an azimuthal projection type meaning that it is based on projection to a plane tangent to the earth’s surface. Gnomonic projection is also known as Gmonic and Central, and it is neither conformal nor equal area. Gnomonic projections are commonly used with radar data, since the radar’s location is suitable as the point tangent to the earth’s surface. It is also a projection which is well-suited when transforming from polar to cartesian coordinate systems. In order for the use of this projection type to be meaningful, a specific Gnomonic projection must be defined for each radar. This eliminates the ability to use Gnomonic projections when compositing radar images. Within the NORDRAD system, Gnomonic images from each radar are defined as a basic product which can then be transformed to other projections for generating higher level products such as composites.

The BRDC uses a Lambert azimuthal equal area projection when creating its image products. As the name suggests, this projection is azimuthal and equal area. The point tangent to the earth’s surface is defined as $20^{\circ}E, 60^{\circ}N$ which is located centrally in the BALTEX Region, in the Åland islands. An advantage of this projection is that it allows for areal integrations of a given variable, due to its equal area nature. A coverage area in this Lambert projection has been defined for each BALTRAD radar (Figure 2.2 and Table 2.1) based on the coverage of its corresponding polar coordinate system. Examples of these coverage areas are provided in the following sections.

The DWD provides its data in a Polar Stereographic projection centred at the north pole, a central meridian of $10^{\circ}E$ and a latitude of true scale at $60^{\circ}N$. A stereographic

projection is another azimuthal projection type. It is conformal, meaning that shapes are correctly represented.

All projections used for storing BRDC products use a spherical earth model with an earth radius of 6 370 997 *m*. The projection used by the DWD assumes an earth radius of 6 370 000 *m*.

All BRDC image products have 2 *km* horizontal resolution and 8-bit depth. Maximum range is 240 *km* unless otherwise stated.

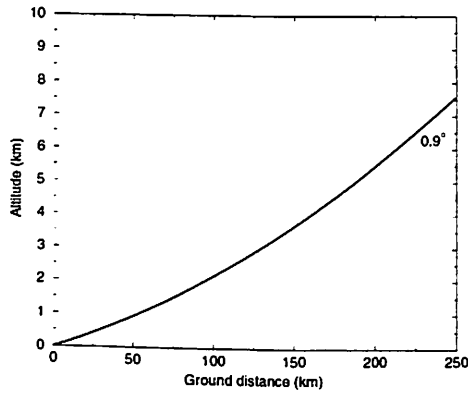
3.2 Cartesian representations of radar data

There are many ways of representing radar data on cartesian surfaces. This section serves to provide a brief introduction to the most common types of 2-D products, since the terminology will be used in subsequent parts of this report.

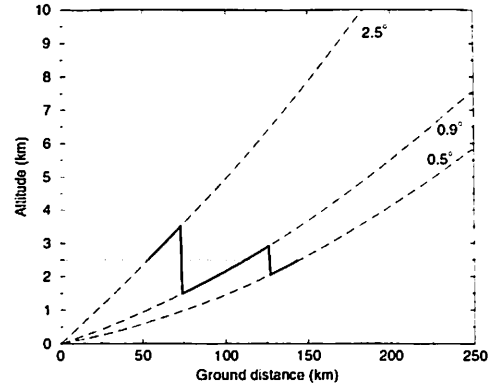
A Plan Position Indicator (PPI) is the simplest of these products, where a single polar scan of data is transformed to a regular cartesian grid. Figure 3.1a illustrates how data from such a scan are located in relation to a cartesian plane along the earth's surface. This Figure also illustrates so-called $\frac{4}{3}$ earth radius radar beam refraction, which is commonly assumed for radar. A brief presentation of radar beam refraction is given in Section 4.2.1.

A Constant Altitude PPI (CAPPI) contains only those polar data which are defined as being located at a specified altitude. It can be seen as a horizontal slice through the polar volume parallel to the sea surface. Due to the normal refraction of the radar beam, a CAPPI will contain data from several scans. This technique is often used at low altitudes (e.g. 500 m above the radar) to reduce permanent ground clutter echoes proximate to the radar. There are several ways of defining how to select polar data based on the specified altitude, the most common of which is to use a nearest neighbour algorithm in areas between where the main axes of the lowest and highest beams intersect the specified altitude (Figure 3.1b). Henja and Michelson (1999) developed an improved strategy where a full 3-D interpolation is conducted; for each cartesian pixel, a horizontal search radius is specified in terms of the output cartesian grid's spacing, and a vertical search distance is specified in terms of a multiple of the given radar's beamwidth. This strategy insures that data are interpolated consistently in the horizontal plane and vertically according to normal radar behaviour. Some of the institutes operating BALTRAD radars use the nearest neighbour algorithm in their operational software; others use some form of 3-D interpolation.

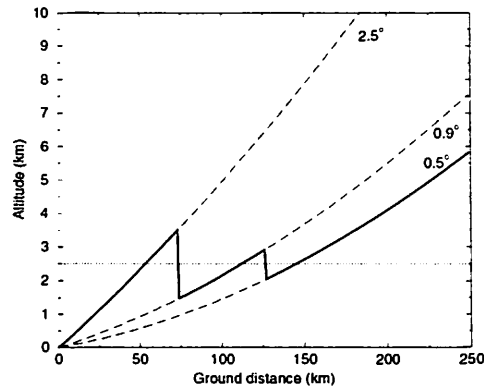
A Pseudo-CAPPI can be defined as "a CAPPI or the closest thing to it". In other words, it is a combination of PPI and CAPPI techniques, where the PPI technique from the highest scan is used close to the radar, the CAPPI technique is used where polar data exist at the specified altitude, and the PPI technique is again used from the lowest scan at the most distant ranges (Figure 3.1c). The Pseudo-CAPPI technique is often used in operational environments since it provides images with



(a) PPI from a 0.9° scan.



(b) 2.5 km CAPPI generated from three scans.



(c) 2.5 km Pseudo-CAPPI generated from three scans.

Figure 3.1: How polar data are located in relation to cartesian surfaces when generating 2-D products with the nearest neighbour method.

the greatest potential to contain information out to maximum operational range, while simultaneously reducing permanent ground clutter near the radar.

3.3 Speckle reduction

Speckle can be defined as individual polar bin or cartesian pixel values surrounded by bins/pixels with no echo. Speckle is usually assumed to be noise which should be identified and removed. A simple despeckling filter has been used on radar data at the BRDC which operates both on polar and cartesian data. Assuming a moving kernel k with odd-valued dimensions i and j centred about a given bin/pixel, the proportion of neighbours with echoes (P_e) is given by

$$P_e = \frac{\sum_{(-i/2) \dots (i/2)} \sum_{(-j/2) \dots (j/2)} 1, k_{(i,j)} \neq noecho}{ij} \quad (3.1)$$

where *noecho* is the value used to flag bins/pixels void of echoes. A threshold t is then used to determined whether the value centred in k is speckle, such that

$$k_{(0,0)} = \begin{cases} noecho, & P_e < t \\ k_{(0,0)}, & P_e \geq t. \end{cases} \quad (3.2)$$

The threshold t used at the BRDC is 0.25 and both i and j are 3. In practise, this means that more than two of nine possible values must be echoes in order for $k_{(0,0)}$ to not be considered speckle.

3.4 DNMI

Data arrives through the NORDRAD system in 8-bit NORDRAD format and Gnomonic projections for each radar. Both non-Doppler and Doppler reflectivity data are received in 2 and 1 *km* horizontal resolution, respectively. These are 500 m Pseudo-CAPPI images described above in Section 3.2. Maximum range is 120 *km* for Doppler and 240 *km* for non-Doppler data. These data are despeckled according to Section 3.3.

Where both Doppler and non-Doppler reflectivity images are available, both are transformed to Lambert projection (Section 3.1) at 2 *km* horizontal resolution and a hybrid Pseudo-CAPPI is generated which consists of the minimum reflectivity value of the two. These two images are illustrated in Figure 3.2 using data from Radar Oslo. Two *km* data are transformed using a nearest neighbour algorithm, whereas one *km* Doppler data are subjected to a bilinear operator when transforming to the 2 *km* output grid. The hybrid technique is intended to minimize both permanent ground clutter near the radar and more distant spurious echoes of various origin which are removed with Doppler signal processing out to 120 *km*. If only Doppler or non-Doppler data are available, then they are despeckled and transformed.

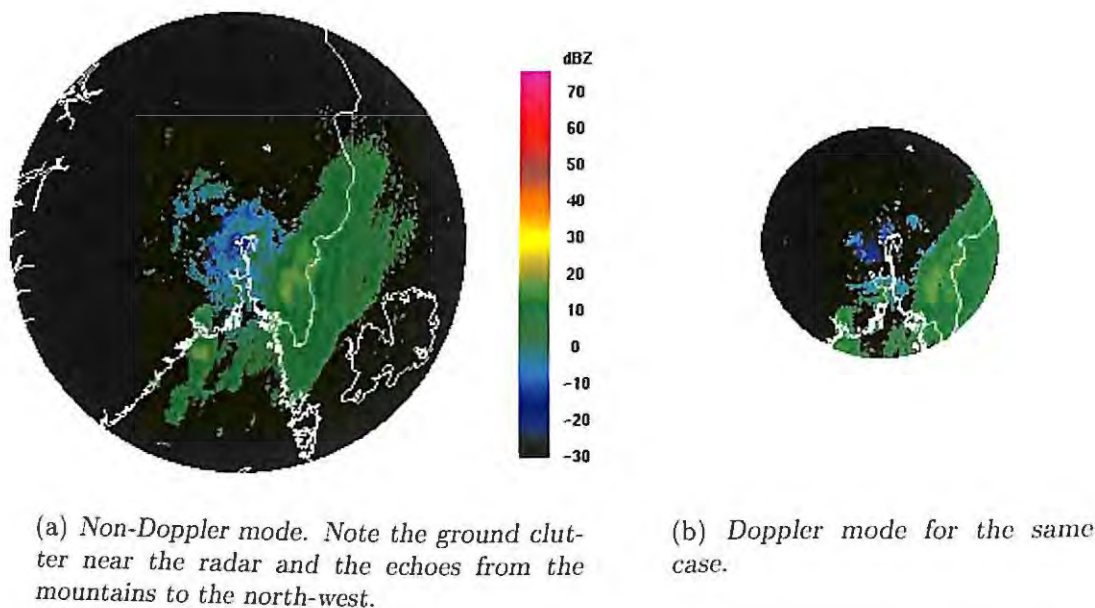


Figure 3.2: Non-Doppler and Doppler images from Radar Oslo used when generating the hybrid Pseudo-CAPPI DBZ product.

3.5 FMI

Data is transferred through the Internet in 8-bit NORDRAD format and Gnomonic projections for each radar. Horizontal resolution is 2 km except for Radar Rovaniemi which has 2.5 km. Maximum ranges are 300 km for Rovaniemi and 250 km for the other radars. These images first despeckled (Section 3.3) and then transformed to the DBZ Lambert projection using a nearest neighbour algorithm.

Note that with the exception of the first 2-3 weeks of the BRIDGE Base-Line Period (October 1-18), data from FMI is processed using Doppler techniques out to full 250 km range.

3.6 SWERAD

The DBZ product is generated directly from original polar volumes where these are available. The first action taken on these volumes is that they are despeckled in polar space according to Section 3.3.

A hybrid Pseudo-CAPPI is generated using the 3-D polar to cartesian transformation methods outlined in Henja and Michelson (1999) (Section 3.2) and Doppler and non-Doppler reflectivity volumes. The horizontal search radius is set to $0.5 \times \sqrt{2}$ output pixels and the vertical search distance is defined as one beamwidth. For each cartesian output pixel, Cressman weights (Cressman 1959) are used to derive separate horizontal (w_h) and vertical (w_v) weights for all input polar values in the

sample. A Cressman weight (w) for a given dimension is defined as

$$w = \frac{(R^2 - r^2)}{(R^2 + r^2)} \quad (3.3)$$

where R is the maximum search distance and r is the distance in the given search direction. A 3-D weight is derived from these two according to

$$w_{3-D} = \sqrt{w_h w_v}. \quad (3.4)$$

The polar volume data are transformed directly to the Lambert projection using this method. For areas containing both Doppler and non-Doppler data, the hybrid product contains the minimum value. If either of the polar volumes is missing, its corresponding 2-D Gnomonic NORDRAD product is used instead when generating the hybrid Pseudo-CAPPI product.

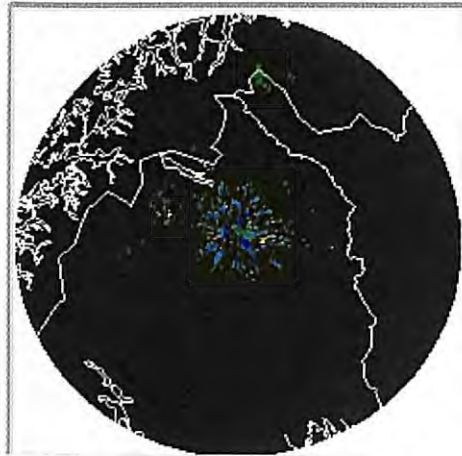
Where polar volumes are not available, a hybrid product of the type presented above in Section 3.4 is attempted. If only Doppler or non-Doppler data are available, then they are despeckled and transformed. Data from Radar Göteborg are not available as polar volumes and are treated directly in this manner.

The appearance of the hybrid product is worth commenting. Figure 3.3a shows a conventional Pseudo-CAPPI product from Radar Kiruna for a case with only one small shower to the north. Permanent ground clutter can be seen in this image at both close and distant ranges. The corresponding hybrid product (Figure 3.3b) is much cleaner and illustrates the technique's ability to use Doppler where it is available. However, SWERAD radars' scan strategies are not standardized, ie. they are not the same among radars and they are different for Doppler and non-Doppler modes. Another complication is that these two modes are calibrated differently. The combination of these two effects can lead to artifacts in hybrid products in the transition between Doppler and non-Doppler data (Figure 3.3c) in cases with precipitation. Such artifacts are deemed less serious than the presence of clutter and are therefore tolerated.

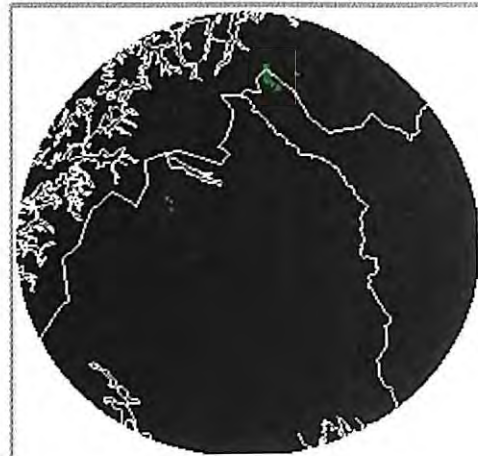
The hybrid technique is only used due to lack of Doppler capability out to full operational range (240 km). Were this capacity available, then the need for collection of non-Doppler data would be reduced or eliminated.

3.7 DMI

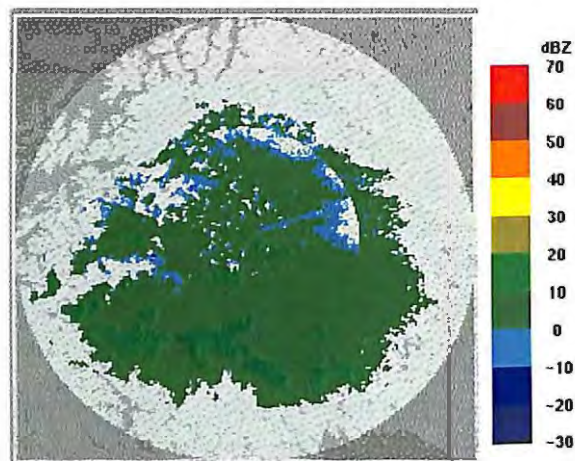
Data from Radars Copenhagen and Sindal arrive through the NORDRAD system. Data from Rømsø are transferred through the Internet. All data is available in 8-bit OPERA BUFR code in each radar's Gnomonic projection. These data are only available in 2 km non-Doppler mode. Temporal resolution is 10 minutes. These times are matched to the 15 minute DBZ product resolution such that data valid for 20 and 50 minutes past the hour are used at 15 and 45 minutes past the hour, respectively.



(a) 500 m Pseudo-CAPPI.



(b) 500 m hybrid Pseudo-CAPPI.



(c) Artifacts in hybrid due to different scan strategies and/or calibration between Doppler and non-Doppler modes.

Figure 3.3: Difference between conventional (a) and hybrid (b) Pseudo-CAPPI products, and artifacts (c) which can appear in hybrid products.

The data from DMI are first despeckled before being transformed to Lambert projection using a nearest neighbour algorithm. Following that, all reflectivity values are reduced by 5 *dBZ*. This is a result of a programming error in the Ericsson calibration software which was discovered as a part of a study commissioned by NORDRAD (Dahlberg 1996). The error has been corrected in Norwegian and Swedish radars, but not in Danish radars. This step is conducted while generating the DBZ product in order to homogenize the values from all BALTRAD radars to a common level.

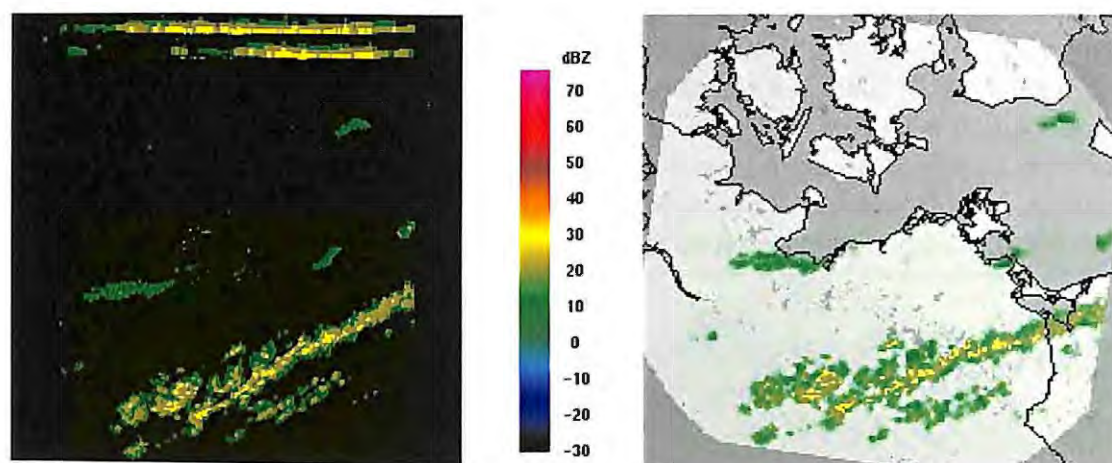
3.8 DWD

Four-bit OPERA BUFR-coded data from German radars arrive through the ECMWF's ETR service. These products are designated "PL" by the DWD and are described in Schreiber (1998). Briefly, this image product is extracted from a three dimensional cartesian volume containing reflectivity factor (*dBZ*) values; the volume's dimensions are $400 \times 400 \times 12$ km and the projection is the polar stereographic one presented in Section 3.1. Input data to the cartesian volume is a 20-scan polar volume. The PL product consists of so-called ground view, side and top projections. The ground view contains the echoes closest to the surface. If there are no or invalid (ie. clutter marked) data in the lowest height level, a valid echo is searched for in higher levels up to a given maximum height (that used operationally is 6 km). During the extraction process the horizontal resolution is reduced from 1×1 km to 2×2 km and the strongest echo of the four pixel is taken for the coarse resolution pixel. The fourth of the four bits is used for denoting clutter. The side and top projections are also known as side panels and these contain the maximum reflectivity factor value for each km of height in the north-south and east-west directions, respectively.

In processing the PL product at the BRDC, a mask is first used to determine which image areas are located within the 230 km maximum range of DWD's radars, since no such information is found in the BUFR files. Everything beyond this range is deemed void of data. The image is then transformed to Lambert projection using a nearest neighbour algorithm before being despeckled.

The PL product (in BUFR) contains quantized precipitation intensity (*mm/h*) data which vary according to summer and winter. The intensity levels from November 1 to March 31 are 0.002, 0.4, 1.9, 8.1, 35.0, and 150.0 *mm/h*. From April 1 to October 31, the lowest intensity is instead 0.06 *mm/h*. Up to November 14, 1999, the BRDC used a lowest intensity of 0.1 *mm/h* regardless of season, since this is the value provided in the BUFR files. From November 15 to December 1, 1999 the seasonal lowest intensity is used regardless of the BUFR files' contents. Using the adjustment method described later in this section, it was discovered that the lowest intensity levels for both summer and winter were both too low to make the results of the adjustment meaningful. As a result, the lowest intensity is once again 0.1 (*mm/h*) as of December 2, 1999.

The Z-R relation used by the DWD is $Z = 256R^{1.42}$ and the intensities are converted to reflectivity factor (*dBZ*) using this information when generating the DBZ product.



(a) PL product. The top few rows are side panels.

(b) DBZ product from the same case.

Figure 3.4: Difference between original German PL and BRDC DBZ products, based on an image from Radar Rostock.

The ensuing issue is how these quantized reflectivity values relate to the 8-bit levels of the Nordic radars. For these purposes a method has been developed which analyses the overlapping areas between Radars Hamburg and Rømø and Radars Rostock and Copenhagen. For each of these pairs, the area of overlap is determined. Then, for each radar in the pair, the mode value of all echoes in the overlapping region is calculated. The mode is that value in the sample which occurs most frequently. Then the average difference between corresponding modes is determined, which is the adjustment factor valid for that time. This adjustment is averaged together with the previous nine factors to arrive at a temporally smoothed adjustment factor, which is then linearly applied to the data from all German radars. The only conditions in deriving the adjustment factor are that:

- data from all four radars must be available, and
- the total number of echoes used to derive the adjustment factor must be at least 10% of the smallest overlapping area, in this case that between Hamburg and Rømø.

If these conditions are not met, then the nine previously-determined adjustment factors are averaged and used.

Figure 3.4 illustrates the way in which the DWD's PL product is processed into a BRDC DBZ product. Since the PL product covers a $400 \times 400 \text{ km}$ area and the radars' maximum ranges are 230 km , the resulting DBZ product appears flat-sided with rounded corners (Figure 3.4b) when transformed to Lambert projection. DBZ products derived from data from the IMGW (Radar Legionowo), and to a lesser extent FMI, have this appearance as well.

3.9 IMGW

The BRDC receives data from Radars Legionowo and Katowice through the Internet at 10 minute temporal resolution and in OPERA BUFR code. These times are matched to the 15 minute DBZ product resolution such that data valid for 20 and 50 minutes past the hour are used at 15 and 45 minutes past the hour, respectively. The products from these two radars differ and are described separately.

The product generated by Radar Legionowo is a 700 m Pseudo-CAPPI which has been quality controlled for clutter and anomalous propagation echoes according to the methods presented in Moszkowicz (1995). Horizontal resolution is 4 *km* and the precipitation intensity values (*mm/h*) are quantized into 139 levels ranging from 0.1 to 400 *mm/h*. Maximum operational range is 240 *km*.

The product generated by Radar Katowice is a so-called MAX-CAPPI which contains the maximum value in the vertical dimension, regardless of scan, for each cartesian pixel in the output grid. Horizontal resolution is 1 *km* and precipitation intensity values (*mm/h*) are quantized into 14 levels ranging from 0.1 to 205.1 *mm/h*. Maximum operational range is 200 *km*.

The Z-R relation used by the IMGW is the classic Marshall-Palmer ($Z = 200R^{1.6}$) (Marshall and Palmer 1948). The precipitation intensities are converted to reflectivity factor (*dBZ*) using this relation before being transformed to Lambert projection using a nearest neighbour algorithm. The images are then despeckled (Section 3.3) before being saved to disk.

4 Composite Images of Radar Reflectivity Factor (DBZC)

This product, designated DBZC, is based on individual DBZ products described in the previous chapter. The DBZC product is designed to be one homogeneous collection of all DBZ images represented as one image for each 15 minute time step. This chapter presents the characteristics of the DBZC product, the compositing algorithm and a quality control procedure used to postprocess the composites.

4.1 Area definition

The DBZC product projection is the Lambert azimuthal equal area projection presented in Section 3.1. The image geometry is summarized in Table 4.1. This image area has been defined such that the most peripheral BALTRAD radar coverage area (in Lambert Azimuthal Equal Area projection) in each compass direction has been used to determine the composite image coverage. These radars are Kiruna to the north, Katowice to the south, Hægebostad to the west and Anjalankoski to the east.

4.2 Compositing algorithms

There are numerous ways of compositing individual images into one. Common to all is the requirement of selecting values from one or more input images for each pixel in the output composite. The selection criteria is commonly one of the following:

- the value is taken from that radar whose antenna is closest to the given composite pixel,
- the maximum value from any of the radars which cover the output composite pixel,
- the value is taken from that radar where the distance from the input pixel to the earth's surface is the shortest,
- the value is taken from that radar whose data was most recently ingested,
- all input pixels covering the same output pixel are averaged,
- the user subjectively defines which radar(s) contribute to which composite pixels,
- combinations of any of the above.

An example of compositing algorithms being used operationally today is the second (maximum value) which is used for composites in the Central European Radar Network (CERAD) (Randeu et al. 1996). Another example is the method being used

Table 4.1: *Spatial and temporal characteristics of the DBZC product.*

Projection	Lambert azimuthal equal area
Horizontal resolution	2 km
Temporal resolution	15 min
Width (pixels)	815
Height (pixels)	1195
Lower (S) left (W) corner (lon)	6.748°
Lower (S) left (W) corner (lat)	47.478°
Upper (N) right (E) corner (lon)	36.243°
Upper (N) right (E) corner (lat)	69.172°

within NORDRAD, which is based on that presented by Andersson (1992a). Here a coarse-resolution digital elevation model (DEM) is used to derive the distance from each pixel in each input image to the earth's surface. This information is combined with each radar's beamwidth for each composite pixel. For Radar Norrköping, an inventory of blocked and partially blocked sectors provides additional information. The compositing algorithm blends the information and arrives at one input pixel value for each output pixel in the composite.

The compositing algorithm used at the BRDC is the "minimum distance to earth" (MDE) one, which is third in the above list. A DEM from the United States Geological Survey (USGS 1999) is used, its horizontal resolution being around 1 km, and its vertical resolution being one m. Using this DEM, the distance from each pixel in each input image to the earth's surface can be calculated.

What follows is a brief presentation of commonly assumed radar beam refraction and how knowledge of it can be used to derive the distance to the surface information used in compositing.

4.2.1 Radar beam refraction

This subsection's content is condensed from Watson (1996); the topic is dealt with comprehensively by Kerr (1951). Electromagnetic waves would travel in straight lines if the atmosphere were homogeneous. Since the permittivity of the atmosphere (ϵ) is stratified, electromagnetic wave propagation is not straight. The atmosphere's refractive index (n) is related to the relative permittivity such that $n^2 = \epsilon_r$. The radio refractive index

$$N = (n - 1) \times 10^6 \quad (4.1)$$

is often used instead of n since small changes in n , caused by different atmospheric water vapour contents, can cause large changes in electromagnetic wave propagation.

Given the height of a ray above the earth's surface (h), the radius of the ray curvature (r), and the vertical refractive index gradient (dn/dh), the horizontal angle of the path (θ) to a given point may be expressed as

$$\frac{1}{r} = \frac{1}{n} \frac{dn}{dh} \cos \theta. \quad (4.2)$$

r may be related to the relative earth radius (R_e) in terms of the refractive index gradient, according to Brussaard and Watson (1995), by

$$\frac{r}{R_e} = k_e \approx \frac{1}{1 + R_e(dn/dh)} \quad (4.3)$$

where k_e is the effective earth radius factor. If the earth radius is assumed $k_e R_e$ then rays can be modelled as propagating in straight lines. Given an earth radius of 6370 km, k_e may be expressed in terms of N as

$$k_e \approx \frac{1}{1 + (dN/dh)/157}. \quad (4.4)$$

The radio refractive index gradient (dN/dh) near the earth's surface is around -40 N/km which gives an effective earth radius factor of $k_e = \frac{4}{3}$. This has given rise to the assumed phenomenon " $\frac{4}{3}$ earth radius radar beam refraction" or "standard refraction".

Regions where $k_e < 0$ are referred to as containing ducts, where rays remain at heights proximate to the earth's surface. Regions where $0 \leq k_e \leq \frac{4}{3}$ are said to be regions of super-refraction, meaning that rays propagate abnormally towards the earth's surface. Regions where $k_e > \frac{4}{3}$ are said to be regions of sub-refraction, meaning that rays propagate abnormally away from the earth's surface.

4.2.2 Distance to the surface

Using the elevation angles for each radar's scan strategy, a polar volume containing height-above-sea-level data can be generated and the corresponding DBZ product containing this height information as well. The USGS DEM mentioned above (transformed to each DBZ coverage area) is then subtracted from the height-DBZ product to arrive at a matching distance-to-surface DBZ product for each BALTRAD radar, which can be saved as a lookup table (LUT) for later generation of DBZC products.

For each radar the radius of ray curvature is given as

$$r' = H_r + \frac{1}{(1/R_e + dN/dh)} \quad (4.5)$$

where H_r is the height of the radar's antenna (*m a s l*) and dN/dh is -39 N/km.

Then, each range bin's height is

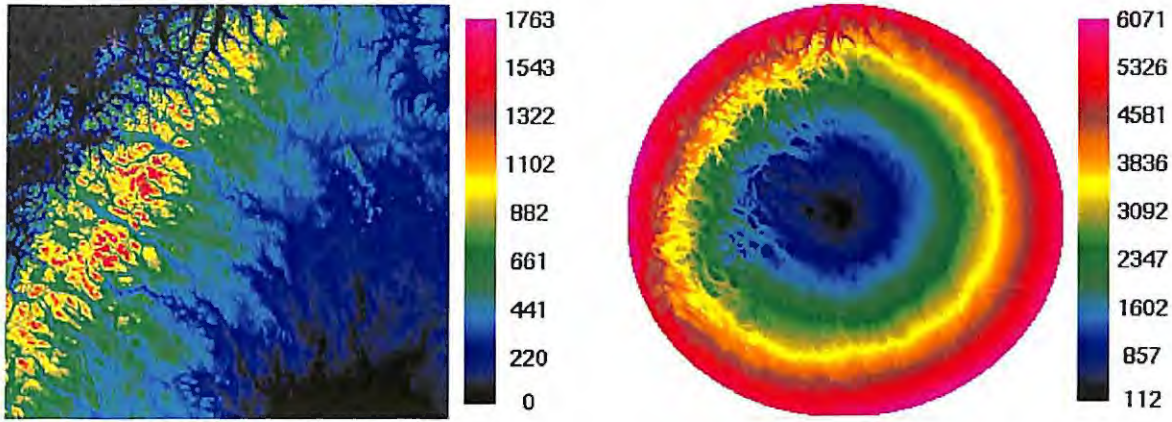
$$H = \sqrt{A^2 + B^2} - r' \quad (4.6)$$

where

$$A = 0.001 + r' + S \times \sin \phi \quad (4.7)$$

where S is the slant range (*m*) and ϕ is the elevation angle for the given scan (radians), and

$$B = S \times \cos \phi. \quad (4.8)$$



(a) Topography (m).

(b) Distance to surface (m).

Figure 4.1: Topography and derived distance to the earth's surface for Radar Kiruna. Geometry as with the DBZ product.

The calculations need only be done for all range bins at the first azimuth gate of each scan. These values are then duplicated for successive azimuth gates until the scan is complete. This is repeated for all elevations until a polar volume containing height data, for generating the height-DBZ product, has been derived.

This algorithm is exemplified in Figure 4.1 which contains the USGS DEM and the distance-to-surface LUT for Radar Kiruna.

4.3 DBZC compositing algorithm

For each BALTRAD radar a distance-to-surface LUT has been generated according to Section 4.2.2. At each 15 minute time step, all DBZ products are collected and their corresponding distance-to-surface LUTs are read. Then, for each pixel in the output DBZC, all DBZ images containing corresponding data are evaluated; the output value (dBZ) is taken from that image whose distance-to-surface LUT value is the lowest.

This MDE algorithm is designed to minimize border effects between radars, since the borders' locations are where two radar beams are the closest to each other in space. This is illustrated in Figure 4.2 which contains a composite with distance-to-surface LUT data. The apparent "ridges" denote the borders between contributing radars. The main factor which determines the location of the border is the radars' heights. In fact, the use of the USGS DEM is not even necessary unless it can be used to determine and flag blocked and partially blocked sectors and include this in the evaluation process. This has not been conducted yet. Unless this is done, the MDE is analogous to selecting the pixel whose height above sea level is the lowest.

As a matter of interest, the total differing area between "closest radar" and MDE algorithms has been determined and it is illustrated in Figure 4.3. This area is

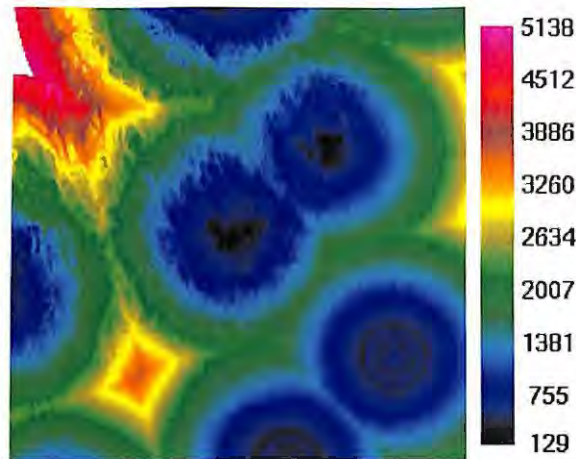


Figure 4.2: *Composite containing distance-to-surface data (m), centred at Radar Leksand and covering the DBZ product area for it.*

around $36\,800\text{ km}^2$ or 1.7% of the total potential area covered by BALTRAD radars. The largest differences are found between radars with the largest vertical distance between their sites.

The use of the “closest radar” compositing algorithm is also thought to reduce border effects between radars since their pulse volumes are very similar at borders between radars. Although it is not objectively determined here, the minimum distance in space between values determined with the MDE algorithm is thought to reduce border effects more than the minimum difference in pulse volumes given with the “closest radar” algorithm.

There remains work to be done on homogenizing data from a heterogeneous network of radars. Despite the progress within the NORDRAD collaboration, which discovered and corrected programming errors accounting for around 7 dB difference between radars operated in Sweden and Finland (Koistinen et al. 1999), there remain systematic differences which require addressing. One known difference is that an attenuation correction tuned for rain is always used in Swedish, Norwegian and Danish radars whereas none is used in Finnish. Since the major proportion of precipitation measured by radar, on an annual and even seasonal basis, is snow (due to the altitude of the measurement being above the melting layer, and the radar cross section of dry snow being much less than that for rain) the value of using this attenuation correction can be questioned if homogeneous data is prioritized.

4.4 Quality control

A postprocessing step is carried out after each composite has been generated. It has been designed to identify and remove echoes in areas where precipitation is judged not to occur. The method is influenced by that presented by Ebert and Weymouth (1999) to identify potential areas without rain-bearing clouds, using geostationary satellite data. Their objective was to use these “no rain” observations together with data from the national gauge network to produce improved daily rainfall analyses.

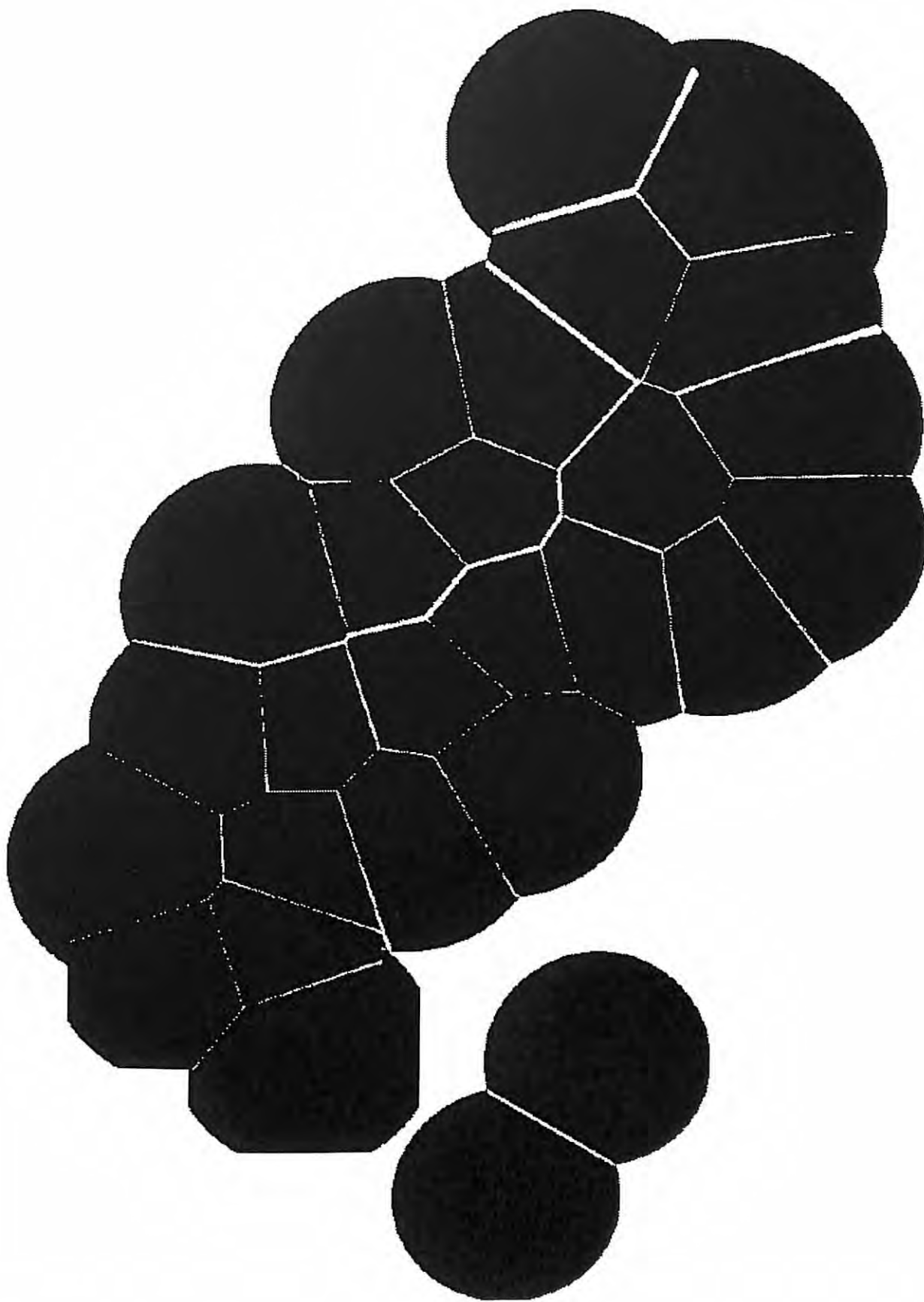


Figure 4.3: *Composite displaying areas between radars in white which differ depending on which algorithm is used: a “closest radar” or the MDE.*

As will be presented in the following, the same concept can be applied to removing “false precipitation” in radar imagery.

Simple thresholding of satellite temperatures has been used in the past to identify potential rain-bearing clouds, but this method becomes problematic if the coverage area contains different climatic regimes since each regime would require a unique threshold. Ebert and Weymouth (1999) instead use expected minimum surface temperatures, based on climatological data, together with Geostationary Meteorological Satellite (GMS) brightness temperature composites. The difference between the surface and brightness temperatures is the basis for identifying areas of no rain and areas with potential for rain.

At the BRDC, this concept has been applied using brightness temperatures from the Meteosat platform available every 30 minutes and hourly 2-m temperatures analyzed with SMHI’s MESAN (Mesoscale Analysis) system (Häggmark et al. 1997). The analysis domain is illustrated in Figure 5.1. MESAN uses the method of optimal (or statistical) interpolation (Daley 1991) to analyze various variables. For the 2-m temperature analyses, the first guess consists of a postprocessed forecast field from the HIRLAM numerical weather prediction model (Källén 1996) or the previous analysis should the forecast field be unavailable. A structure function which is based on the relationship among temperature, water content and altitude above sea level is used in the interpolation (Häggmark et al. 1997). MESAN fields are interpolated to a rotated lon/lat grid with a resolution of 0.2° .

Meteosat-b IR data is received at SMHI, calibrated, navigated, and rectified to a polar stereographic projection using the VCS system (VCS 1995). The output area covers northern Europe with a pixel size of 8 km. No corrections are made to the image content for errors associated with the sensor’s oblique viewing angle at high latitudes. This temperature imagery is rectified to the MESAN 2-m temperature field’s grid using bilinear interpolation.

Since Meteosat data is available every 30 minutes and MESAN every hour, the matching of data is done such that Meteosat data from the bottom of each hour is matched to the MESAN data from the top of the same hour. If no MESAN field is available for the given hour, then the previous hour’s field is used if available.

Potential areas with precipitating clouds ($\Delta T = 0$) are identified if any of the following conditions are met:

$$\Delta T = 0, \begin{cases} T_{2m} - T_s \geq 20 \\ T_{2m} < -5^\circ C \\ T_s < 0^\circ C \end{cases} \quad (4.9)$$

where T_{2m} is the 2-m analyzed temperature and T_s is the satellite’s brightness temperature. Otherwise $\Delta T = 1$.

When matching DBZC products with the ΔT mask the composites from 0 and 15 minutes past the hour are matched with the mask at the top of the hour; the composites from 30 and 45 minutes past the hour are matched with the mask at the bottom of the hour.

All radar echoes where $\Delta T = 1$ are removed. These echoes are not flagged; they just receive the equivalent “no echo” value which is equal to the lowest reflectivity factor value.

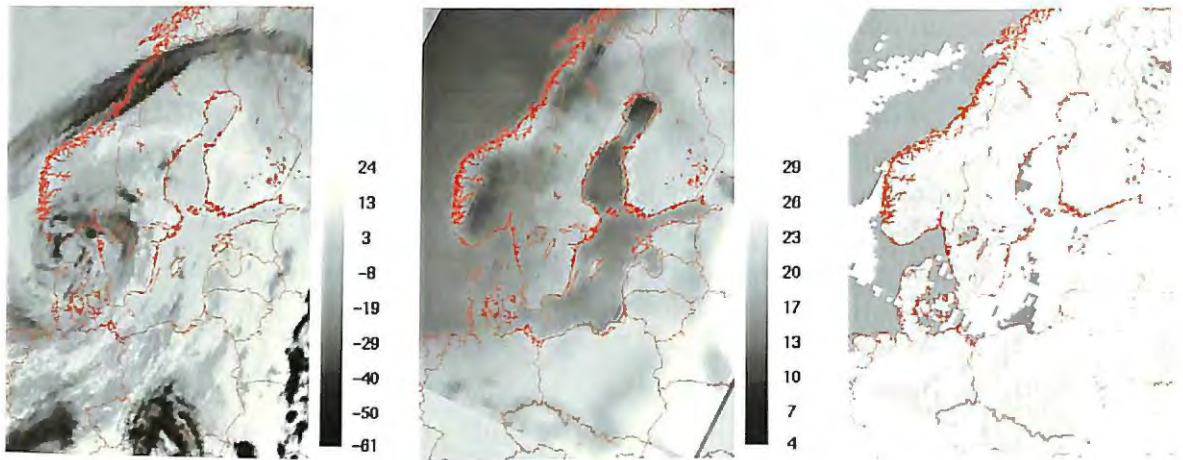
4.4.1 Method performance and limitations

The basis for a discussion of the ΔT mask’s performance is a case from June 10, 1999 at 13:00 UTC, illustrated in Figure 4.4. A low with small-scale showers, centred between Denmark and Norway, was moving slowly southwards. The radar imagery from this case contains a number of noteworthy features. At the time, FMI’s radar data were not subject to any Doppler processing; the images from Finnish radars thus contain significant ground clutter, system noise and anomalous propagation echoes from the Estonian coast. The Swedish radars also contained some clear air echoes and the Latvian and Lithuanian coasts can be discerned from Radar Hemse (Figure 4.4d). Two-metre temperatures are relatively high in southern Finland and mid-Sweden (Figure 4.4b), while brightness temperatures are also relatively high (Figure 4.4a).

As can be seen in the the ΔT mask and the filtered composite (Figure 4.4c and e), the method is successful in identifying most of the false precipitation. The difference threshold of 20° results in a limited proportion of spurious echoes remaining while a small amount of genuine precipitation from the low in southwestern Scandinavia is also removed. This may indicate a need to use a more conservative threshold, since it may be considered more important to retain precipitation at the cost of also keeping more false precipitation.

This method contains a number of limitations which should be brought to light. The horizontal resolution of the Meteosat and MESAN data are much coarser than that of the radar imagery. This makes small-scale convective precipitation difficult to treat properly, since such convective cells may only fill part of a Meteosat pixel. The result is an increased risk that such genuine precipitation be removed. Compounding the problem is the coarser nominal resolution of the satellite data with increasing latitude, along with geometrical offsetting of clouds due to the sensor’s oblique viewing angle. While the frequency of small-scale convection is lower with increasing latitude, this issue should be kept in mind since the southernmost part of the BALTEX Region is at around $49^\circ N$, where significant convection is known to take place during summer.

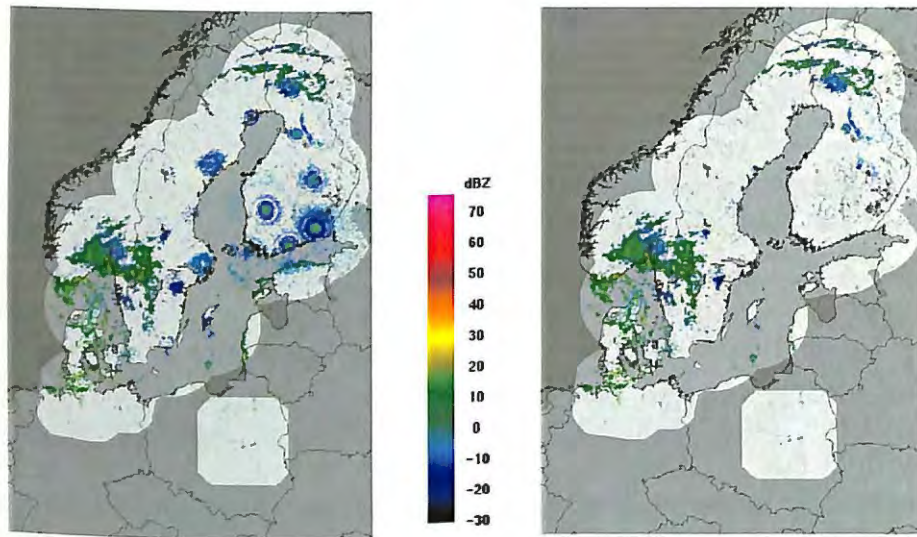
The issue of climate plays an important role as well. A prerequisite for the method to work is that the 2-m temperature is higher than the satellite’s brightness temperature. This is often not the case during the colder seasons where snow and ice-covered surfaces are common. During such conditions it can be impossible to discriminate between clouds and the earth’s surface based on temperature information; this problem is well known even with much higher resolution satellite data with several spectral channels (Karlsson 1996). Even in less extreme situations, the temperature difference may simply not be large enough for the method to work, which is why it is combined with the two conservative static thresholds as



(a) Meteosat brightness temperature ($^{\circ}\text{C}$).

(b) 2-m analyzed temperature ($^{\circ}\text{C}$).

(c) ΔT mask.



(d) Unfiltered DBZ.

(e) Filtered DBZ.

Figure 4.4: Derivation and application of the ΔT mask in quality control of the DBZC product. June 10, 1999 at 13:00 UTC. Note that temperature shading is cold (dark) to warm (light).

a “failsafe”. This means that the ability of the method to succeed deteriorates with decreasing 2-m temperature data. It should, however, be kept in mind that the greatest problems with anomalous propagation echo contamination occur during warm seasons (Alberoni et al. 2000) and this is when the ΔT mask can be derived and used with acceptable confidence.

Although it has not been objectively determined, it can be concluded that the ΔT method provides a robust means of identifying and removing spurious radar echoes and that this method appears to work acceptably when the conditions require it.

5 Systematic Correction of Gauge Observations

Precipitation gauges are commonly viewed as providing accurate point measurements. There are, however, a number of well-known error sources which can strongly influence their accuracy. According to Førland et al. (1996) these error sources are:

- wind error
- evaporation error
- wetting error
- splashing/drift error
- site error
- instrument error
- observer and unforeseen errors

The largest of these problems is the wind (flow distortion) error, especially in snow where losses can be high despite many gauges being equipped with wind shields. Together with the evaporation and wetting errors, it constitutes the most serious of the systematic errors. It is vital that such errors are corrected prior to the measurements' use in quantitative applications. The errors in the measurements risk otherwise being propagated to the applications using such measurements.

If an inventory of the characteristics of each gauge site is properly conducted, then information on systematic factors influencing the quality of gauge measurements can be used to correct such measurements. While this may have been done on the national level in one or more countries in the BALTEX Region, it certainly has not been done in all of them. The implication is that a systematic correction applicable to datasets for the BALTEX Region cannot be conducted using detailed information on each gauge site.

An implementation of the Førland et al. (1996) Dynamic Correction Model (DCM) has been carried out at the BRDC which makes use of operationally analyzed fields produced by SMHI's MESAN (Mesoscale Analysis) system (Häggmark et al. 1997) along with 12-hour gauge observations available from the synoptical weather station network (SYNOP) at 6 and 18 UTC each day. Since the BRDC does not operate in real time, the use of MESAN fields which are valid for the same times as BRDC products is feasible. It should be noted, however, that the implementation of the DCM could also work with such fields produced an hour earlier or with forecast fields produced from the HIRLAM numerical weather prediction model (Källén 1996). The DCM implementation is presented in the following.

Table 5.1: Gauge types and shields used operationally in the BALTEX Region. Note that the default gauge type for other countries than those listed here is Hellmann.

Gauge type	Shield type	Country
SMHI	Nipher	Sweden, Norway
Geonor	Alter	Sweden
H&H-90	Tretyakov	Finland
Hellmann	None	Denmark, Germany, Poland, Other
Tretyakov	Tretyakov	Russia, Estonia, Latvia, Lithuania, Belarus, Ukraine

Table 5.2: Daily evaporation loss constants for each gauge type (mm/day). These values are divided by 24 to arrive at hourly losses.

Month	SMHI	H&H-90	Hellmann	Tretyakov
January	0.02	0.03	0.01	0.03
February	0.03	0.04	0.02	0.04
March	0.04	0.06	0.03	0.05
April	0.12	0.20	0.04	0.22
May	0.10	0.04	0.09	0.13
June	0.15	0.05	0.15	0.15
July	0.15	0.05	0.16	0.15
August	0.10	0.05	0.08	0.10
September	0.05	0.04	0.02	0.05
October	0.03	0.03	0.01	0.03
November	0.03	0.03	0.01	0.03
December	0.02	0.03	0.01	0.03

Table 5.3: Wetting constants per case (mm/12 hours) for each gauge type and precipitation phase. These values are divided by the number of hours with precipitation per 12 hour SYNOP term.

Precip. phase	SMHI	H&H-90	Hellmann	Tretyakov
Liquid	0.07	0.13	0.14	0.14
Solid	0.02	0.05	0.10	0.09
Mixed	0.06	0.11	0.18	0.14

Table 5.4: Gauge constants for liquid and solid precipitation for each gauge type and case (mm/12 hours).

Precip. phase	SMHI	H&H-90	Hellmann	Tretyakov
Liquid	-0.05	-0.05	0.0	-0.05
Solid β_0	-0.08871	-0.07556	0.04587	-0.04816
Solid β_1	0.16146	0.10999	0.23677	0.13383
Solid β_2	0.011276	0.012214	0.017979	0.009064
Solid β_3	-0.00877	-0.007071	-0.015407	-0.005147

5.1 Gauge types in the BALTEX Region

Førland et al. (1996) conducted their study with gauges used operationally in the Nordic region. Rubel and Hantel (1999) implemented the DCM for correcting daily gauge measurements and extended its use to the BALTEX Region. These gauges are the SMHI, Geonor, H&H-90, Hellmann, and Tretyakov, the characteristics of which are given in Table 5.1 along with the countries which use them. While Sweden uses both SMHI and Geonor gauge types, the DCM implementation presented here assumes that all Swedish gauges are of the SMHI type.

Daily evaporation loss constants for each gauge type are found in Table 5.2, wetting constants for each gauge type are found in Table 5.3, and gauge coefficients defined in the next Section are found in Table 5.4.

5.2 Dynamic Correction Model

The Førland et al. (1996) DCM estimates the corrected precipitation P_c as

$$P_c = k \cdot (P_m + \Delta P_W + \Delta P_E) \quad (5.1)$$

where k is the correction factor,
 P_m is the measured precipitation,
 ΔP_W is the wetting loss according to Table 5.3, and
 ΔP_E is the evaporation loss according to Table 5.2.

In determining k the precipitation phase must be taken into account, and so k for liquid and solid phases have been defined. The correction factor for liquid precipitation k_l is given by

$$k_l = \exp[-0.00101 \cdot \ln(I) - 0.012177 \cdot v_g \cdot \ln(I) + 0.034331 \cdot v_g + 0.007697 + c] \quad (5.2)$$

where I is the rain intensity (mm/h),
 v_g is the wind speed (m/s) at gauge height, and
 c is the gauge coefficient given by Table 5.4.

For solid precipitation, the correction factor k_s is

$$k_s = \begin{cases} \exp[\beta_0 + \beta_1 \cdot v_g + \beta_2 \cdot T + \beta_3 \cdot v_g \cdot T], & v_g > 1.0 \text{ m/s} \\ 1.0, & v_g \leq 1.0 \text{ m/s} \end{cases} \quad (5.3)$$

where β_i are the gauge coefficients given in Table 5.4,
 v_g is the wind speed (m/s) at gauge height, and
 T is temperature ($^{\circ}C$).

Note that this equation (5.3) was established using a data set where $1.0 < v_g \leq 7.0 \text{ m/s}$ and $T \geq -12^{\circ}C$. This makes the validity of Equation 5.3 unknown in stronger winds and/or colder temperatures. The equations' sensitivities are presented and discussed in Section 5.4.

Given situations with mixed phase precipitation, the correction factor k_m becomes

$$k_m = \frac{(r_l \cdot k_l + r_s \cdot k_s)}{(r_l + r_s)} \quad (5.4)$$

where k_l and k_s are the correction factors for liquid (Eq. 5.2) and solid (Eq. 5.3) precipitation and r_l and r_s are the precipitation amounts in liquid and solid form, respectively.

5.3 Input variables

The difficulty in implementing the DCM is in getting ahold of the variables it requires. In applying the DCM to 12-hourly SYNOP precipitation sums, each site commonly reports temperature and wind speed, yet valid only for that point in time when the measurement is made. Not all of these sites report more frequently than every 12 hours, which makes the determination of temperatures and wind speeds, not to mention rain intensity, for the duration of each 12-hour SYNOP term difficult if they are solely based on point observations. The DCM implementation carried out by Rubel and Hantel (1999) assumes access to a high density network of climate stations; in correcting precipitation measurements from this dataset, those stations lacking DCM variables take them from the closest station with them. If, however, analyzed fields are available at regular intervals instead, they provide an easily manageable and internally consistent alternative. The variables can be taken from the corresponding pixel in the analyzed fields. Stations outside the analysis domain remain, however, uncorrected. The MESAN domain is illustrated in Figure 5.1.

The hourly MESAN temporal resolution implies that each given 12-hour SYNOP term can be broken down into hourly components, where correction factors can be derived and applied to all components where precipitation occurs. The final 12-hour precipitation becomes a sum of corrected hourly precipitation sums, each derived according to Equation 5.1.

Based on this strategy, the derivation of both the rain intensity (I) and the hourly precipitation sum (P_i) for each hour in the term (mm/h) become simply

$$I, P_i = \frac{P_m}{\sum_{i=1}^{12} 1, P_{mes_i} \geq 0.1} \quad (5.5)$$

where P_{mes_i} is the analyzed precipitation sum (mm) for each hour in the term according to MESAN. While it may seem odd to use a precipitation analysis, valid for the same point in time as the gauge observations, to correct the gauge sums which then could be used in an analysis, it should again be pointed out that the lack of a real-time constraint allows this. Also, the input data to hourly MESAN precipitation analyses comes largely from other observation systems. In a real-time scenario, I and P_i could be derived from forecast fields, they could be estimated from previous MESAN analyses, or radar images could be used.

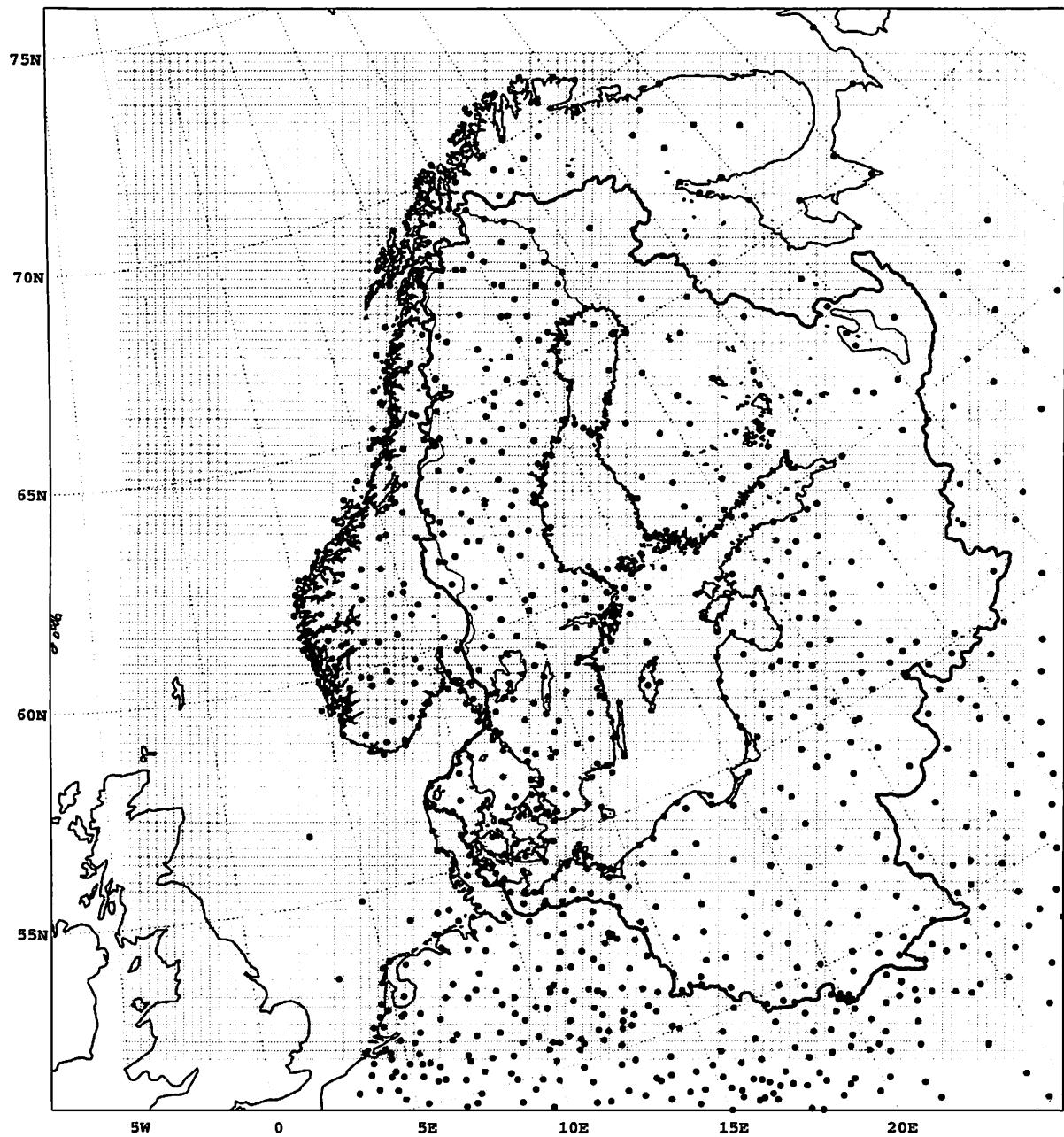


Figure 5.1: The operational MESAN domain in grey. Horizontal resolution is 0.2° on a rotated lon/lat grid. SYNOP stations and the Baltic Sea's catchment area are also illustrated.

In deriving the proportion of snow in measured precipitation, a relationship between the surface wet bulb temperature (T_{iw}) and proportion of snow has been derived in MESAN, based on a large body of synoptical observations from January-March, 1995, as

$$p_{snow} = \begin{cases} 1.0, & T_{iw} < -0.21 \\ 1.0 - \frac{\exp((T_{iw}-1.1) \cdot 3.5)}{1.0 + \exp((T_{iw}-1.1) \cdot 3.5)}, & -0.21 \leq T_{iw} \leq 2.42 \\ 0.0, & T_{iw} > 2.42. \end{cases} \quad (5.6)$$

T_{iw} is an analyzed MESAN variable. The T_{iw} thresholds -0.21 and 2.42 represent 99% and 1% snow contents, respectively. This method of determining the proportion of snow is used in this implementation of the DCM.

Wind speeds operationally analyzed in MESAN are done so for the height of 10 m. The bias is determined between MESAN wind speeds for the latest hour of the given 12-hour SYNOP term and the measured winds reported at that SYNOP term: the MESAN winds are adjusted according to this bias. The WMO (1994) logarithmic wind reduction equation is given as

$$v_g = (\log(hz_0)) \cdot (\log(Hz_0)) \cdot (1 - 0.024\alpha) \cdot v_H \quad (5.7)$$

where h is the gauge height (m) above the ground,

z_0 is the roughness length (m),

H is the height of the wind speed measurement (m),

v_H is the wind speed (m/s) measured at height H , and

α is the average vertical angle (degrees) of obstacles around the gauge.

Assuming a common gauge height $h = 1.5$ m, an average roughness length $z_0 = 0.25$ m, the analyzed wind speed height $H = 10$ m, and $\alpha = 1$ (unknown), this wind reduction reduces to a constant factor 0.49, which is used in this implementation.

The remaining input variable is temperature, where the MESAN 2 m temperature is used.

5.4 Sensitivities of the correction equations

In order to evaluate the performance of this DCM implementation, a number of tests can be carried out which serve to describe and illustrate the behaviour of the equations. The goal is to determine the magnitudes of the correction factors given different meteorological conditions.

For the purposes of these tests, the constants in Table 5.4 for the SMHI gauge type are used. Also, a common surface pressure of 1000 hPa is assumed and all values of P_m are valid for 12 hours.

The first test is to determine the influence of temperature on k , given constant wind speed (1.1 m/s) and different values for P_m . Relative humidity is set to 90% and the temperature interval is from -2 to 5°C. The results are illustrated in Figure 5.2

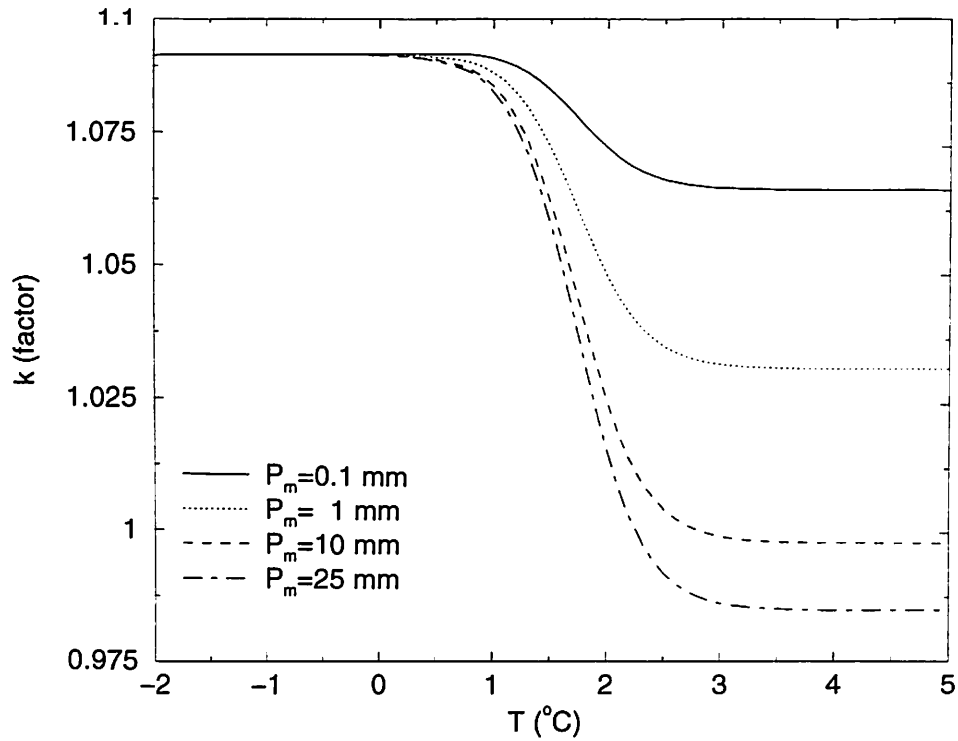


Figure 5.2: Correction factor (k) as a function of temperature (T) for different precipitation sums (P_m).

where it can be seen that k is only marginally affected by temperature given weak wind conditions. The shapes of the curves are determined by the proportion of snow (P_{snow}) which is derived from the wet bulb temperature (T_{iw}). The maximum variation in k , around 10%, applies to the highest measured accumulation.

Another factor influencing k is the precipitation intensity (I) in liquid phase. Assuming all liquid precipitation the influence of I on k can be determined for different temperatures. This is illustrated in Figure 5.3 where it is clear that I influences k about as much as T does. The only real differences in k occur between 1 and 3°C. At temperatures at or greater than 4°C, I causes differences in k up to around 7%.

The wind error is known to have the greatest influence on gauge measurements and it is therefore of interest to determine how this influence is corrected with this DCM implementation. This was tested by assuming a constant P_m of 5 mm and deriving k for various wind speeds (v_g) and temperatures. These results are shown in Figure 5.4, confirming the extreme differences in k given different conditions. In -10°C and 20 m/s winds, the method assumes that over 99% of the precipitation (blowing snow) misses the gauge, and this compensation increases with increasing wind speed. At temperatures at and above 5°C and wind speeds of 20 m/s, the correction assumes that just over 50% of the precipitation has missed the gauge, but this correction is nowhere near that applied to lower temperatures. For lower wind speeds, these plots correspond well to that prepared by Førland et al. (1996) for the SMHI gauge type. This confirms that the most important error is the flow distortion error and that its correction is based on wind speed.

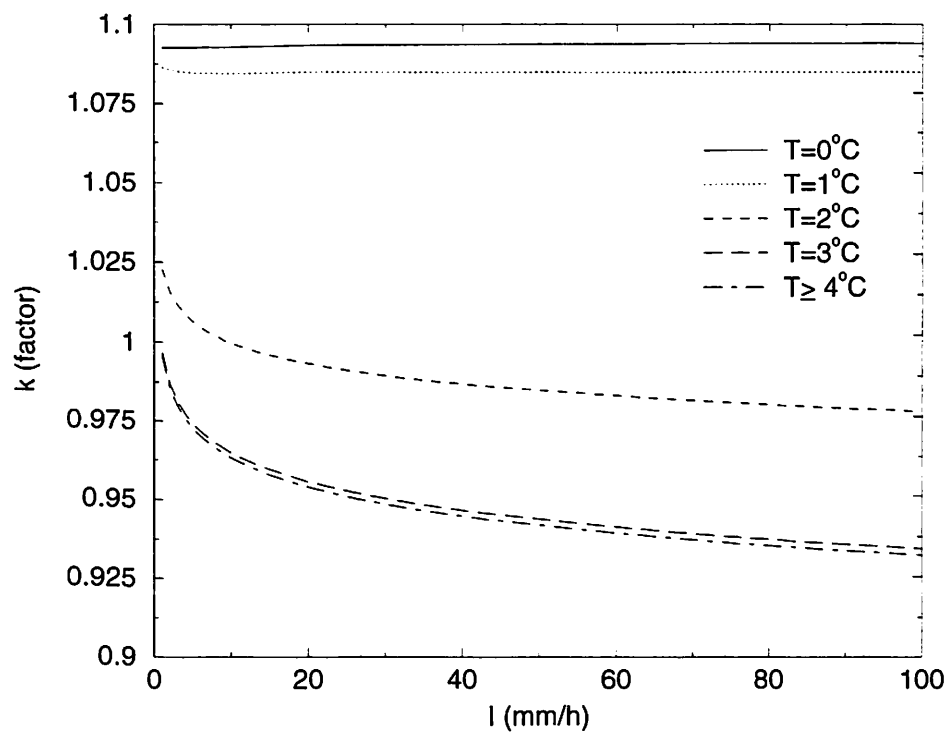
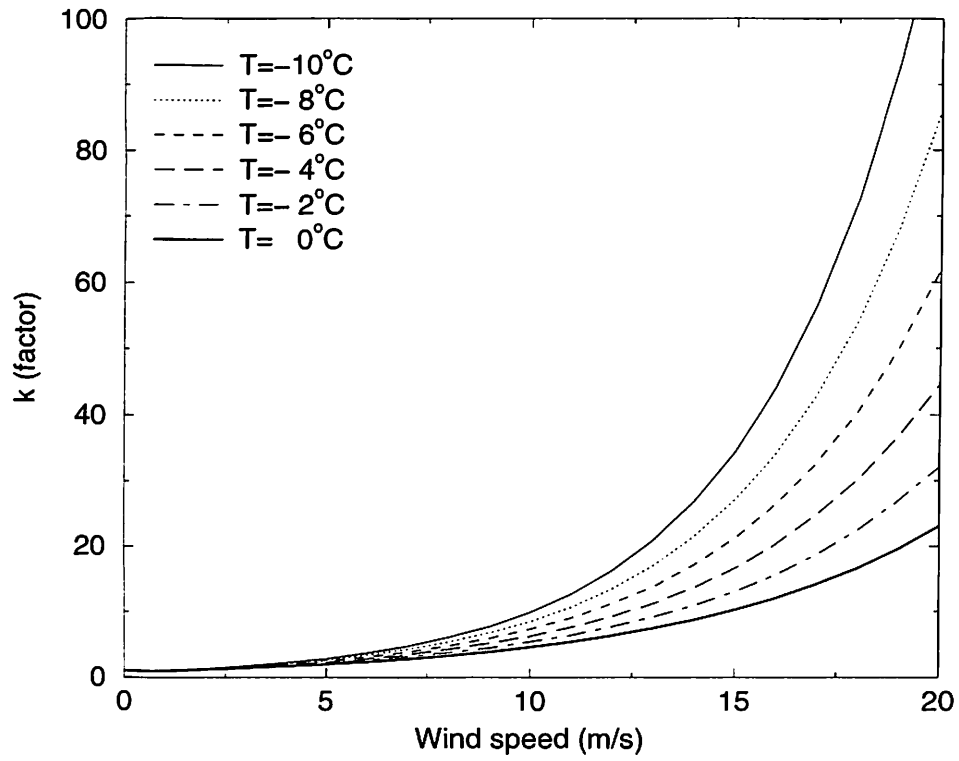
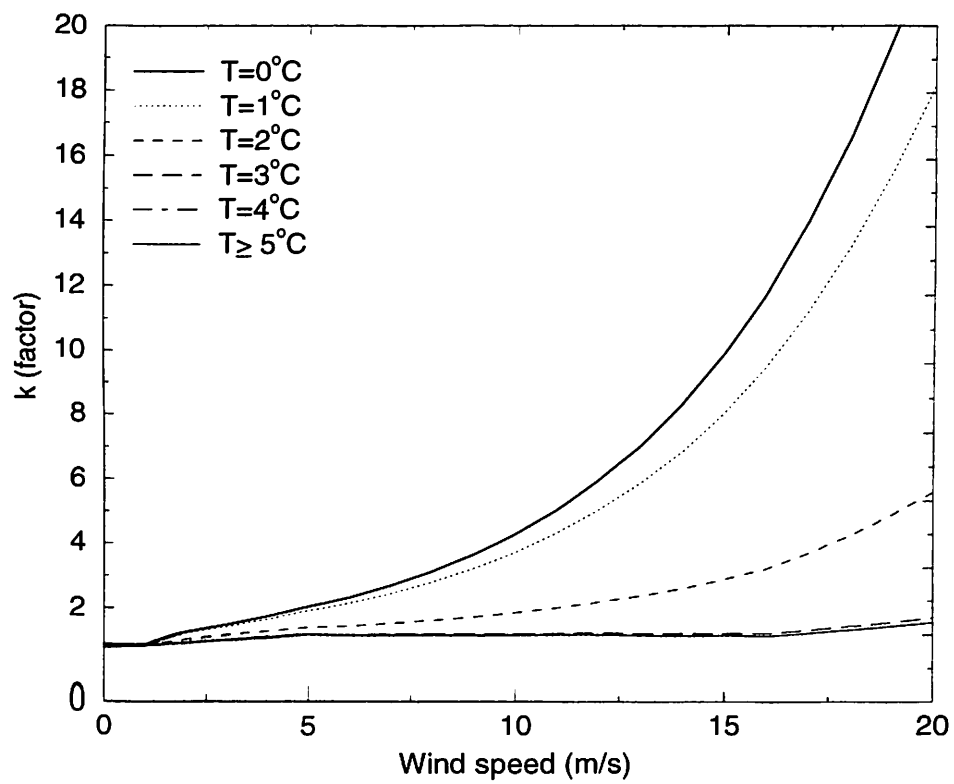


Figure 5.3: Correction factor (k) as a function of precipitation intensity (I) for different air temperatures (T).



(a) Cold temperatures.



(b) Warm temperatures.

Figure 5.4: Correction factor (k) as a function of wind speed (v_g) for different temperatures (T). Note the difference in scale between the two plots.

6 Accumulated Precipitation (RR)

This product, designated RR, is based on individual DBZ products described in Chapter 3 and gauge observations corrected according to the method presented in Chapter 5. The RR product is designed to contain the highest quality observation-only based precipitation analysis at the original high resolution provided by BAL-TRAD radars.

This Chapter presents the method used to generate the RR product, along with the characteristics of the product itself. The overall objective of the method is to preserve the spatial detail in radar data while adjusting it quantitatively using gauge observations, the idea being that a gauge adjustment will minimize the bias between radar and gauge data and minimize the range dependency on the radar measurements. In areas of relatively high gauge density, the gauges will influence the adjustment more; in areas with low gauge density, the overall relation between gauges and radar will have the greatest influence on the final adjustment.

6.1 Temporal integration periods

Both three and twelve-hourly RR products are generated. The three-hourly products are generated for 0, 3, 6, 9, 12, 15, 18, and 21 UTC, whereas the twelve-hourly products are generated for 6 and 18 UTC which corresponds with the 12-hourly terms used with global synoptic observations (SYNOP) exchanged through the Global Telecommunications System (GTS).

6.2 Area definitions

The RR product projection is, like the other products, the Lambert Azimuthal Equal Area projection presented in Section 3.1. Two product areas are defined which correspond with the three and twelve-hourly analyses. The three-hourly analyses are generated to the DBZC composite area whose image geometry is summarized in Table 4.1. The twelve-hourly analyses incorporate SYNOP data and so an area covering the Baltic Sea's drainage basin has been defined. The image geometry of this area is summarized in Table 6.1.

6.3 Gauge radar adjustment background

The methods used to adjust radar sums with gauge data are based on research conducted in various places over the last several decades. Originally, Barnes (1964) presented a method for objective analysis (interpolation) of variables to two-dimensional regular grids. Barnes (1973) improved the method and its efficiency for use with time-series data. Brandes (1975) applied this method together with radar data and introduced some enhancements. A few years later, Koistinen and Puhakka (1981)

Table 6.1: *Spatial characteristics of the 12-hourly RR product. The characteristics of the 3-hourly RR product are given in Table 4.1.*

Projection	Lambert azimuthal equal area
Horizontal resolution	2 km
Width (pixels)	835
Height (pixels)	1134
Lower (S) left (W) corner (lon)	10.136°
Lower (S) left (W) corner (lat)	48.511°
Upper (N) right (E) corner (lon)	43.050°
Upper (N) right (E) corner (lat)	67.896°

improved upon Brandes' implementation in ways which will be explained later in this Chapter. Common to these methods is that they are based on a spatial adjustment of a relationship based on the gauge-to-radar ratio (G/R). A review of these and other methods for gauge adjustment of radar data is provided in Barbosa (1994).

Following Koistinen and Puhakka (1981), there a number of assumptions which have to be made when conducting a gauge adjustment of radar data. These are:

- Gauge measurements are accurate for the gauges' locations. By subjecting gauge observations to the systematic correction presented in Chapter 5, the quality of these observations can be considered high.
- Radar successfully measures relative spatial and temporal variabilities of precipitation. This issue encompasses the problems of identifying and removing spurious echoes caused by clutter, anomalous propagation, insects, birds, the sun, military jamming, chaff, etc. The use of Doppler processing where available, combined with quality control using the mask based on analyzed 2-m and satellite temperature information (Chapters 3-4), renders radar data with higher quality than if these methods were not used. This should lead to higher quality gauge adjusted results.
- Gauge and radar measurements are valid for the same locations in time and space. This is not true. Gauges provide point values and radars provide spatial integrations often at significant heights above the earth's surface. This assumption must nevertheless be made and the issue is dealt with implicitly when deriving relationships between G/R and distance from the radar.
- Relationships based on comparisons between gauges and radar(s) are valid for other locations in space and/or time. Little is known of this issue but it is an assumption which must be made in order to be able to conduct the three hour analyses, since these are based on adjustment factors determined for the previous 12-hour analysis.

Most previous G/R -based gauge adjustment techniques have been applied to data from individual weather radars and high density gauge networks. For the purposes

of BALTEX, it has been necessary to conduct gauge adjustment using data from a network of radars and a relatively low density gauge network (SYNOP). The five primary innovations of the adjustment technique applied at the BRDC can be summarized in the following points.

- Radar sums are managed as composites.
- Individual radar sums are subjected to a preliminary adjustment to normalize their content to a common level throughout the network. This step is also designed to minimize the bias between radar and gauge sums at each radar site due to systematic errors such as differences in calibration..
- G/R point pairs are collected in a moving time window to ensure a large enough sample such that the risk of overfitting in the relation with distance is minimized.
- A second order polynomial between $\log(G/R)$ and distance from the radar is the basis for the adjustment, whereas Koistinen and Puhakka (1981) based their adjustment on a linear relation.
- The gauge adjusted radar sums are integrated with results of an optimal interpolation of corrected gauge sums in areas without radar coverage.

The methods are presented in more detail in the following sections.

6.4 Accumulated precipitation from radar

Radar precipitation sums are generated for each individual radar, using the DBZ products. Three-hourly sums are integrated into individual images for generating the three-hourly analysis. These three-hour sums are in turn used when generating the twelve-hourly analyses. The reason for summing individual radars is that any given radar in a large, heterogeneous network can malfunction and not provide data for a given 15 minute interval. This means that many areas in a composite containing summed precipitation may contain data from more than one radar if the DBZC products are summed. As will be presented later in this Chapter, the knowledge of which pixel in a given sum composite originates from which radar is imperative, since preservation of the systematic errors inherent to each radar's data is initially desired. A simple and efficient means of insuring that this knowledge is retained when creating these sum composites is to first create sums for each radar and then composite them. This is what has been done when generating the RR product, as systematic errors inherent to each radar's data are preserved.

6.4.1 Three hour sums

For creating the three-hourly sums, all DBZ images from each radar are collected for the given three hour period. Each one of them is then quality controlled using the

method involving the ΔT mask presented in Section 4.4. In conducting this step, the ΔT mask, in its original coarse-resolution rotated grid, is transformed to each radar's area using a nearest neighbour algorithm before being applied. The idea behind this is to minimize the errors to areal precipitation accumulations which are caused by spurious echoes.

Each quality controlled image is then converted from reflectivity factor (dBZ) to precipitation intensity (mm/h) using a static $Z - R$ relation. For colder months (October-March) the relation is $Z = 400R^{2.0}$. For warmer months the relation is $Z = 200R^{1.5}$. For the given three hour period, an average precipitation intensity image is derived which is then multiplied by three to arrive at three-hourly accumulated precipitation. The only constraint in deriving the average intensity is that at least 75% of the possible input images (9 of 12) must be available. Otherwise, that individual radar is rejected.

Once the three-hourly sums for each radar have been derived, they are composited using the MDE algorithm presented in Section 4.3.

It should be noted that no sums are generated using data from Radars Norrköping and Luleå, and these radars are thus excluded from the RR product. This is due to significant problems with blocked and partially blocked sectors from these radars, associated with poor siting, which have not been treated. Excluding them from the RR product is a drastic measure yet it is thought that using them would lead to lower quality products.

6.4.2 Twelve hour sums

Twelve-hourly sums consist of those three-hourly sums comprising each twelve hour period for each radar. The only constraint is that at least 75% of the input three hour sums (3 of 4) must be available. Otherwise, that individual radar is rejected.

Once the twelve-hourly sums have been derived for each radar, they are composited using the MDE algorithm presented in Section 4.3.

6.5 G/R point pairs and their relationship with distance

The gauges used for adjusting radar are those available on-line through SYNOP, within a geographical quadrilateral defined by south-western coordinates $3^\circ E/45^\circ N$ and north-eastern coordinates $45^\circ E/73^\circ N$. The number of gauges varies between 1100-1200, only a small fraction of which observe precipitation during a given 12-hour SYNOP term.

Since the fundamental relationship between G/R and distance¹ is based on a second

¹Where previous works have derived relationships between G/R and slant range (the atmospheric distance from the radar), the method presented here relates G/R with the distance along the earth's surface from the radar, which is slightly different. No significant difference in these two

order polynomial, it is important that the sample of G/R point pairs be large enough, and that their distances be spread throughout the possible range of distances (0-240 km). If this is not ensured, then any derived relations may be physically unrealistic yet statistically significant. An attempt at avoiding this type of overfitting has been made by collecting G/R point pairs throughout a moving seven-day time window and using these to derive the relationship with distance. Point pairs with gauges values under 0.5 or radar sums under 0.1 mm are excluded beforehand. The physical reasoning for this relationship with distance is due to the need for a generalized treatment of the vertical reflectivity profile. Seven days is a sufficiently long period to obtain enough point pairs to calculate a reliable relation most of the time. However, periods during which totally different air masses influence the region will lead to unrepresentative yet unharmed relations, due to the temporal averaging effect.

For each 12-hour SYNOP term, the relation between $F \equiv \log(G/R)$ and distance (r) is derived such that

$$F_r = a + br + cr^2 \quad (6.1)$$

where coefficients a , b and c are determined using a least squares fit. The motivation for using a second order polynomial is that doing so enables non-linear relations. An example of such a situation is where a melting layer (or bright band) would cause a minimum in $\log(G/R)$ at a significant distance from the radar (Figure 6.2). While such relations are more statistically than physically based, they still allow a more realistic fit than would be the case if linear relations were used.

The distance information is taken from a distance composite ($R_{(i,j)}$) which is generated based on those radars which have contributed to a given 12-hour sum composite. So, for each 12-hour sum pixel, there is a co-located distance value. The radar sum values used when deriving F_r are the corresponding pixel values to each SYNOP gauge location; no spatial averaging or “best fit” of the radar sum to the point location is conducted.

Using the coefficients derived according to Equation 6.1, a quality control of the individual observations is conducted whereby they receive a weight according to their quality. The quality is determined by comparing each observed value with its corresponding F_r value such that

$$q_g = \begin{cases} 1, & |z_g| \leq \sigma \\ 1 - (|z_g| - 1), & \sigma < |z_g| \leq 2\sigma \\ 0, & |z_g| > 2\sigma. \end{cases} \quad (6.2)$$

where σ is the standard deviation, z_g is the normalized residual given by

$$z_g = \frac{F_g - \bar{F}_g}{\sigma} \quad (6.3)$$

where F_g is each $\log(G/R)$ value, and \bar{F}_g is the average $\log(G/R)$ value. Observations where $q_g = 0$ are rejected and a new F_r is calculated using the quality controlled point pairs. This quality control procedure is illustrated in Figure 6.1. It is slightly

approaches' results should be noticed.

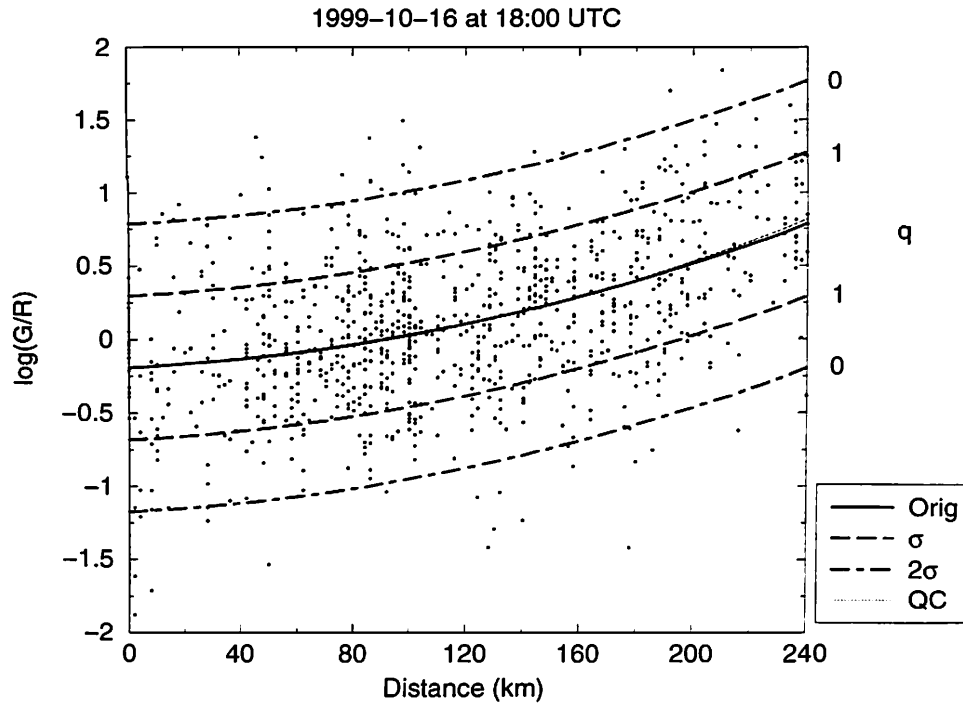


Figure 6.1: Derivation of F_r and quality control of point pairs collected from a seven-day period. Quality weights (q) decrease linearly between one and two standard deviations (σ). The quality controlled relation (QC) differs marginally from the original (Orig) in this case.

different from the approach taken by Koistinen and Puhakka (1981) in that they simply rejected observations outside a given confidence interval.

A new F_r is calculated using the quality controlled point pairs.

At this point the significance of the relation is evaluated using a Student's t-test and a 95% confidence interval. If significant, the coefficients a , b and c , along with the distance composite mentioned above, are used to create a spatial field containing adjustment factor as a function of distance ($F_{r(i,j)}$). If not significant, then there is no influence from distance and so \bar{F}_g is instead used as a constant.

An analysis of the spatial decorrelation distance is also derived using the temporally integrated F_g observations. This is conducted such that all observations' distances to each other are calculated and points are grouped into 10 km intervals up to a maximum of 200 km. For each 10 km interval, the explained variance (r^2) among all observations is determined. The decorrelation distance (D_0) is then estimated as twice the distance at which $r^2 = 1/e$. This is arrived at through linear interpolation of the r^2 values from the two nearest quantized distance intervals.

Before continuing with the derivation of the spatial adjustment factor field, only those N observations from the latest SYNOP term are retained; all others from the seven-day integration period are removed.

6.6 Spatial adjustment factor field

A modified Barnes' analysis of a spatially variable adjustment factor field ($F_{(i,j)}$) is performed. The adjustment factor for each pixel in the field becomes a weighted mean of N observations such that

$$F_{(i,j)} = \sum_{g=1}^N w_{g(i,j)} F_g / \left(\sum_{g=1}^N w_{g(i,j)} \right) \quad (6.4)$$

according to Brandes (1975). The weighting function $w_{g(i,j)}$ is analytically derived as

$$w_{g(i,j)} = \exp(-r_{g(i,j)}^2 / 4k_{(i,j)}) \quad (6.5)$$

where $r_{g(i,j)}$ is the distance between pixel i, j and observation g , and k is the so-called filtering parameter.

Before the actual Barnes' analysis can be carried out, a number of spatial variables must be determined.

The first of these variables is the filtering parameter k which is used to control the degree of smoothing. Brandes (1975) used constant values but Koistinen and Puhakka (1981) pointed out that doing so is only effective if the gauge density is constant. Since the mean spacing within most gauge networks is highly variable, the use of a constant k leads to loss of information in areas with high gauge density and artificial noise in areas with low gauge density. Koistinen and Puhakka (1981) thus allowed k to vary in space as a function of observation density, and their approach has been used here as well.

An estimate of the local observation density for each pixel in the analysis grid is determined as

$$D_{p(i,j)} = \sqrt{a_{p(i,j)} / p} \quad (6.6)$$

where $a_{p(i,j)}$ is the area of a circle including p observations around pixel i, j . Given $p = 5$, the estimate lies within 80-120% of the real observation density, assuming locally constant gauge spacing, which can be considered acceptable. The quality of the point pair values should also be taken into account in determining this estimate; this is done such that $a_{p(i,j)}$ becomes the area of a circle which includes those observations whose qualities (Equation 6.2) sum to at least p .

The next task is to derive a matching field containing $4k_{(i,j)}$ values using the local observation density in $D_{p(i,j)}$. This is calculated through

$$4k_{(i,j)} = -\lambda_{(i,j)}^2 \ln(\delta') / \pi^2 \quad (6.7)$$

where $\lambda_{(i,j)} = 2D_{p(i,j)}$, but is never smaller than twice the grid spacing. The δ' parameter is derived iteratively and is related to the desired resulting analysis response (δ) to wavelength $\lambda_{(i,j)}$ such that

$$i_{(n+1)} = \delta'_{(n+1)} (1 + \delta'^{-0.7}_{(n+1)} - \delta'^{0.3}_{(n+1)}) \quad (6.8)$$

where

$$\delta'_{(n+1)} = \delta'_{(n)} + (\delta - i_{(n)}) / 2 \quad (6.9)$$

while $|\delta - \iota_{(n)}| > 0.01$. Parameters $\delta'_{(n=1)}$ and $\iota_{(n=1)}$ are initialized to 0.5 and 0, respectively. In order to preserve a relatively high amount of detail in the analysis, δ is set to 0.8. This has the effect of retaining 80% of all pattern variations whose size (wavelength) is $\lambda_{(i,j)}$; larger patterns will mostly be retained and smaller patterns will mostly be smoothed out.

Once the $4k$ field has been generated it is used to derive the first guess adjustment factor field ($F_{(i,j)}$) according to Equation 6.4. Then, for each F_g point, its corresponding value is interpolated from the $F_{(i,j)}$ field according to

$$\hat{F}_g = F_g - \sum_{n=1}^4 F_{(i,j)} \frac{1/r_n}{(\sum_{n=1}^4 (1/r_n))} \quad (6.10)$$

where n in this case are the four closest observations to point g and $r_{n=1...4}$ are their distances from F_g . The \hat{F} points are then used to generate an $\hat{F}_{(i,j)}$ field using Equation 6.4 where, this time,

$$w_{g(i,j)} = \exp(-r_{g(i,j)}^2 / 4k_{(i,j)}cp) \quad (6.11)$$

and cp is the convergence parameter which is set to 0.3. This results in a spatial field containing difference (or error) information. By adding $\hat{F}_{(i,j)}$ and $F_{(i,j)}$, the result contains the complete spatially analyzed adjustment factor field which can be called $F_{s(i,j)}$.

The last step is to merge the uniform distance-dependent adjustment factor field ($F_{r(i,j)}$) with the spatially analyzed adjustment factor field ($F_{s(i,j)}$) to derive a final adjustment factor field, such that

$$\bar{F}_{(i,j)} = F_{r(i,j)} + w_{s(i,j)}(F_{s(i,j)} - F_{r(i,j)}) \quad (6.12)$$

where

$$w_{s(i,j)} = \exp(-D_{p(i,j)}/D_0). \quad (6.13)$$

The weight $w_{s(i,j)}$ applied to $F_{s(i,j)}$ is thus controlled by the analyzed decorrelation distance's (D_0) relation to the estimated observation density ($D_{p(i,j)}$) at each pixel of the output grid; the spatial adjustment is given that proportion of the total weight which the local observations can support.

The adjustment of the original radar composite sum ($R_{(i,j)}$) then becomes

$$R_{r(i,j)} = R_{(i,j)} 10^{\bar{F}_{(i,j)}}. \quad (6.14)$$

This gauge adjusted radar product is thresholded such that accumulated precipitation under 0.1 mm is truncated to zero.

6.7 Radar normalization through preliminary adjustment

One of the main problems of conducting a gauge adjustment of composited radar sums is that differences in the accumulations between any two overlapping radars

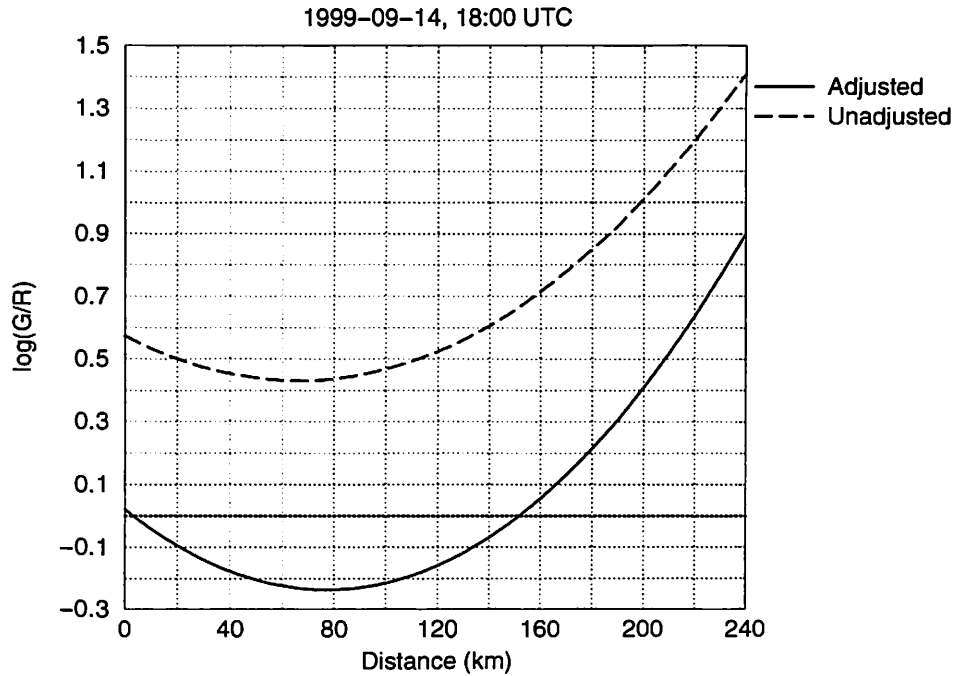


Figure 6.2: *Effect of preliminary adjustment on the derivation of F_r from all radars.*

may be caused by systematic differences in the radars' electrical calibration levels. The result of such differences manifests itself in the form of border effects where two radars meet in composite sums. Unless this phenomenon is dealt with, gauge adjustment risks amplifying border effects in unadjusted composites.

We have implemented an application of the gauge adjustment technique which is designed to normalize radar sums to a common level and to identify and minimize the bias between radar and gauge levels prior to spatial adjustment.

Given a comparison of several (2-3) months of accumulated precipitation from gauges and from individual radars, the relation between $\log(G/R)$ and distance according to Equation 6.1 will be generally valid. In other words, F_r will not be representative for an individual precipitation event but, rather, for precipitation in general. If a comparison is made for each radar in a network using the same integration period, then coefficient a in Equation 6.1 will reflect the general bias between gauge sums and radar sums at each radar site. Coefficient a can then be used instead of $\bar{F}_{(i,j)}$ in Equation 6.14 to normalize the sums from each radar before generating composite sums. The ensuing spatial adjustment will be almost entirely devoted to minimizing the range dependency on the radar sums.

This strategy has been tested and implemented using the months of April and June, 1999, and gauge accumulations from the Swedish climate station network. Both of these months were exceptionally rainy throughout Sweden. Radar data from Swedish radars and Radar Copenhagen were used. Once coefficient a for each radar was derived, these values were in some cases slightly modified to further reduce differences between radars in composite sums. This was done after visual inspection revealed some remaining biases in the composited radar sums. The values of a are

Table 6.2: Preliminary adjustment coefficients (a) for individual radar sums prior to spatial gauge adjustment, along with the number of gauge-radar point pairs (n) and the percentage of radar data available for the comparison.

Radar	a	n	% radar data
Karlskrona	0.6	174	99.2
Göteborg	0.69	207	97.5
Hemse	0.69	117	94.2
Norrköping	0.8	265	99.2
Arlanda	0.27	185	99.2
Leksand	0.64	239	99.2
Hudiksvall	0.5	202	94.2
Örnsköldsvik	0.56	162	95.8
Östersund	0.68	173	96.7
Luleå	1.17	95	95
Kiruna	0.8	73	95.8
Oslo	0.69	—	—
Copenhagen	0.69	114	—
Sindal	0.45	—	—
Romø	0.69	—	—
Hamburg	0.69	—	—
Rostock	0.69	—	—
Berlin	0.69	—	—
Rovaniemi	1.07	—	—
Utajärvi	0.27	—	—
Ikaalinen	0.27	—	—
Kuopio	0.27	—	—
Korpo	0.27	—	—
Vantaa	0.27	—	—
Anjalankoski	0.27	—	—
Legionowo	0.69	—	—
Katowice	0.69	—	—

given in Table 6.2 along with the number of point pairs used in deriving them.

The average value of a (0.693) is used where a could not be specifically calculated, or where it has not been manually modified. Since data from Swedish Radar Arlanda corresponded rather well with that from Finnish Radar Korpo prior to preliminary adjustment, the same adjustment factor was used for all Finnish radars except Radar Rovaniemi.

Note that this strategy should be considered speculative at present and that a more comprehensive analysis of coefficient a , incorporating climate station data from the BALTEX Meteorological Data Centre for application to all BALTRAD radars, should result in more dependable preliminary adjustment factors and information on whether there is a seasonal dependency on them. This should be a future research task.

The effects on F_r due to preliminary adjustment are illustrated in Figure 6.2. In this case from mid-September, 1999, a melting layer has been revealed in the derived relations. Before preliminary adjustment, there is a clear bias between gauge and radar sums of around factor 0.57 at zero distance. After preliminary adjustment the bias has been minimized to around factor 0.02 which also reflects a successful normalization of the radar sums.

In any case, the preliminary values suggest underestimation of 2.7-11.7 dB in the Swedish radars. The value of 5 dB at Radar Hudiksvall is much higher than was observed during the calibration field tests (Koistinen et al. 1999). The reasons behind this discrepancy are unknown and are subject to future research.

6.8 Example case

A 12-hour analysis from February 7, 2000, at 18 UTC is used to illustrate and describe the gauge adjustment technique. The area under scrutiny is that covered by Radar Arlanda, just north of Stockholm. On this occasion a low had its centre over the Norwegian Sea, resulting in mild air and precipitation moving in over the BALTEX Region from southwest to northeast. Most of the precipitation fell in liquid form in the south and in solid form in the north. A largely contiguous area of frontal precipitation was followed by an area of small-scale showers.

The relation between gauge and radar sums derived according to Equation 6.1 was calculated using 1440 point pairs, 67 of which ended up being rejected in the quality control. This was conducted after the preliminary adjustment was carried out using the method presented in Section 6.7. When the distance dependency was determined, the uniform distance-dependent adjustment factor field (F_r) was generated; this field is illustrated in Figure 6.3a. A minimum value of -0.28 indicates that the radar sums at zero distance to the radar are significantly higher than the equivalent gauge levels as a result of the preliminary adjustment. This indicates that the preliminary adjustment served to normalize the radars' levels but it did not minimize the bias between radar and gauge levels. This is probably due to the preliminary

adjustment coefficients having been derived from rain conditions, whereas the case from February 7 contained both snow and rain. Radar and gauge levels are equal at around 60 *km* distance and radar levels lie under gauge levels beyond this distance.

In generating the spatial adjustment factor field, the estimated observation spacing (D_p) is illustrated in Figure 6.3b. Note that the unit is expressed in “mean distance among p points”, and not the more conventional “points per area”. The regular geometrical features are an artifact caused where areas in the image exchange the most distant of the p points. This effect propagates to other spatial parameters used in the adjustment. Minimum (47 *km*) and maximum (150 *km*) mean spacings correspond to areas of 2 209 and 22 500 *km*² per observation, respectively, which indicates relatively low densities. When the D_p field is then used to generate the $4k$ field (Figure 6.3c), the values end up covering a larger range, although the appearances of the two fields are very similar. The areas with the highest levels in both fields are located over the Baltic Sea, which is expected.

When the spatial adjustment factor field (F_s) is generated (Figure 6.3d), it contains values which range between -0.35 and 1.01 which is the same order of magnitude as the uniform distance-dependent adjustment field. The areas where values of F_s are high correspond roughly with areas where values of F_r are high. Areas where values of F_s are low correspond well with the open water of the Baltic Sea. Likewise, the weight assigned to F_s (Figure 6.3e) is lowest over open water, although the values of w_s are low in general. This can be attributed to the low value of D_0 in this case (21.5 *km*). In such conditions, where the decorrelation distance is relatively low, it is reasonable to assign low weights to F_s due to increasing uncertainties in the representativity of the gauge and radar samples arising from small scale features. The result is that the influence given individual observations is reduced with decreasing values of D_0 .

The final adjustment field (\bar{F}) is virtually indistinguishable from the F_r field in this case, so we have instead visualized the difference between the two in Figure 6.3f. Differences are indeed very small. Areas with high negative difference values reflect relatively high weights assigned to F_s , which in turn reflects a relatively greater influence from individual observations arising from a closer proximity to them.

A comparison of the actual accumulated precipitation information produced from the different methods is also illustrated in Figure 6.4. The radar sum composite, subject to no adjustment, is seen in Figure 6.4a. Note the border effect caused by differences in levels between Radar Arlanda, on which the images are centred, and Radar Hemse to the south. This systematic difference is minimized after preliminary adjustment (Figure 6.4b) and the radars' levels are raised significantly, especially proximate to the radars. Although the border between Radar Arlanda and Hemse was successfully treated, border differences between other pairs of radar have not been entirely reduced, which indicates a need for future method enhancements. With the complete gauge adjustment, the dependency on distance is taken into account and levels at short distances are lowered while those at far distances are raised.

By comparison, an image containing an optimal interpolation (OI) of corrected gauge observations only (Section 6.10) shows that the SYNOP network is only able to

capture the gross features of the precipitation pattern over land. The clear difference between adjusted radar and OI over the Baltic Sea indicates that SYNOP gauges are unable to reflect even gross precipitation patterns in these areas.

6.9 Three hourly adjustment

Thus far, the presentation of the gauge adjustment technique has focused around generating the 12-hour RR product. The three-hour RR product does not make use of SYNOP gauge observations since there are too few of them which report at such a high temporal resolution. This presents the challenge of performing a gauge adjustment without gauges.

The strategy adopted at the BRDC is a pragmatic one, where the coefficients a , b and c from Equation 6.1 are saved after each 12-hour analysis and used in the following four three-hour analyses. In these cases, the uniform distance-dependent adjustment factor field ($F_{r(i,j)}$), based on the saved coefficients, is used instead of the final adjustment factor field ($\bar{F}_{(i,j)}$) in Equation 6.14. The individual radar sums are subjected to a preliminary adjustment according to the method in Section 6.7 prior to uniform distance-dependent adjustment. The resulting R_r product is thresholded such that accumulated precipitation under 0.1 mm is truncated to zero.

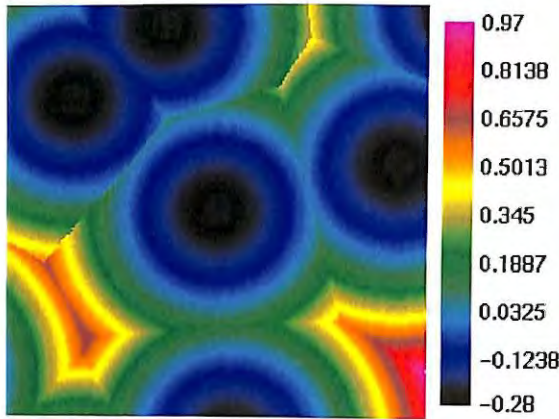
6.10 Treatment of areas without radar coverage

The Baltic Sea's drainage basin does not yet have complete radar coverage, even when data from all BALTRAD radars are available. This presents the problem of filling in the areas of the output RR grid where there is no adjusted radar data available. This is a problem which cannot be resolved without access to alternative observations to radar. In the case of the three-hourly analyses, there is no treatment and areas without radar coverage remain void of information.

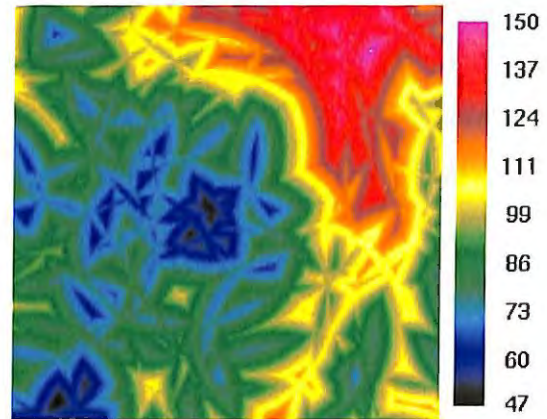
For the 12-hourly analyses, gauge observations are available and they can be interpolated to the whole output grid. The issue then becomes one of choosing an appropriate interpolation algorithm. As has been presented previously in this report, the operational implementation of an optimal (or statistical) interpolation algorithm is included in SMHI's Mesoscale Analysis (MESAN) system. Optimal interpolation (OI) is presented and discussed by Daley (1991), and its implementation in MESAN by Häggmark et al. (1997).

At the BRDC, this OI algorithm is used to interpolate systematically corrected (according to Chapter 5) 12-hourly gauge observations to a regular grid. The output rotated lon/lat grid is the same as that illustrated in Figure 5.1 but with a grid spacing of 0.1°. A zero first guess (or background field) is used. The OI uses an isotropic Gaussian structure function defined as

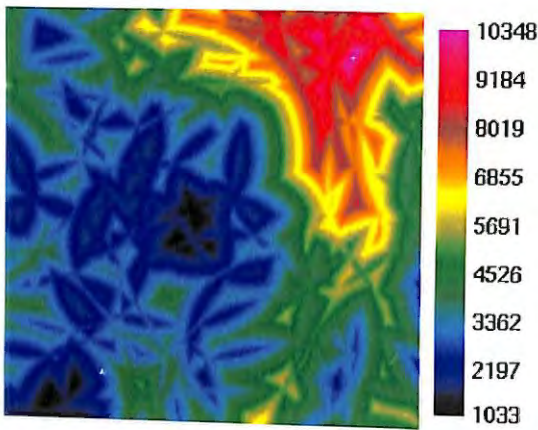
$$r = 0.5 \exp\left(-\frac{d}{D_0}\right) + 0.5 \left(1 + 2 \left(\frac{d}{D_0}\right)\right) \exp\left(-2 \left(\frac{d}{D_0}\right)\right) \quad (6.15)$$



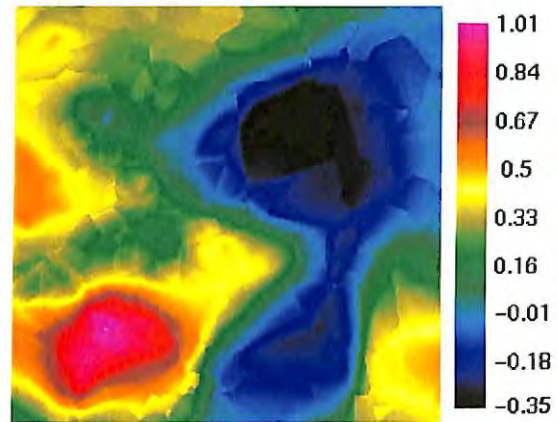
(a) Uniform distance-dependent adjustment factor F_r .



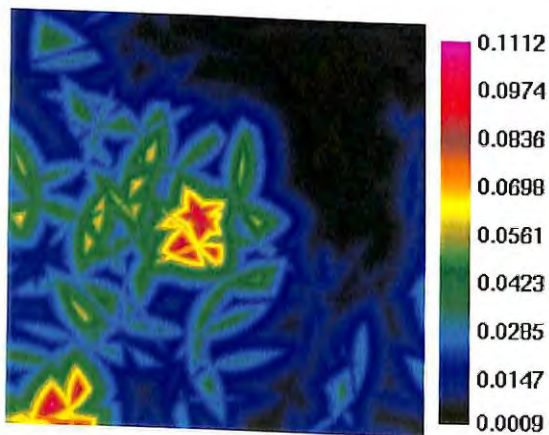
(b) Mean observation spacing D_p (km).



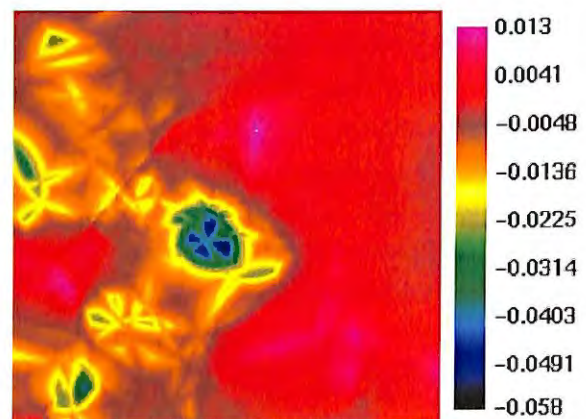
(c) Filtering parameter $4k$.



(d) Spatial adjustment factor F_s .



(e) Weight w_s assigned to F_s .



(f) $F_r - \bar{F}$.

Figure 6.3: Selected spatial parameters, for Radar Arlanda's coverage area, for 12-hour gauge adjustment of radar sums. February 7, 2000, 18 UTC.

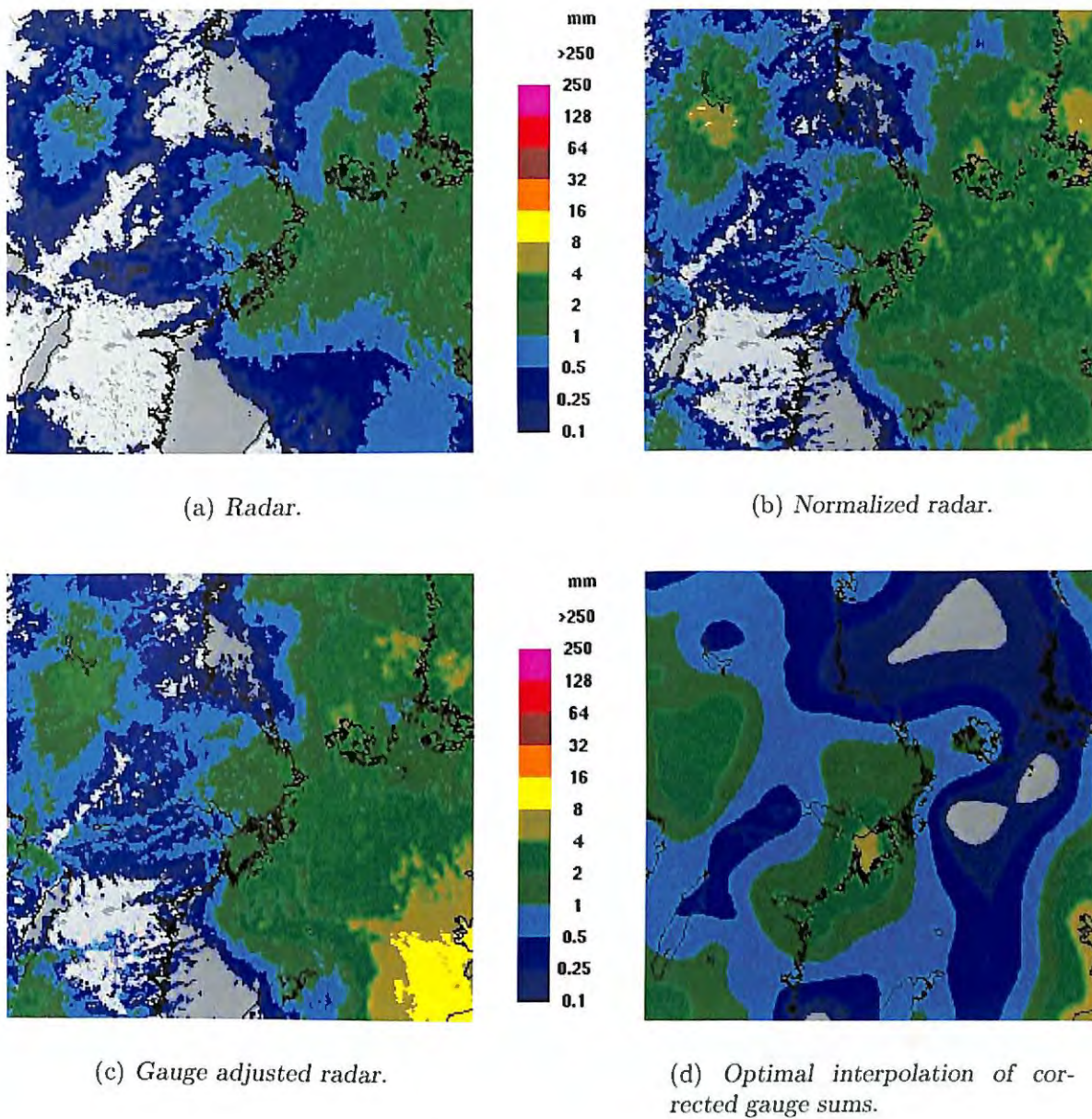


Figure 6.4: Comparison of 12-hour accumulated precipitation using different methods. February 7, 2000, 18 UTC.

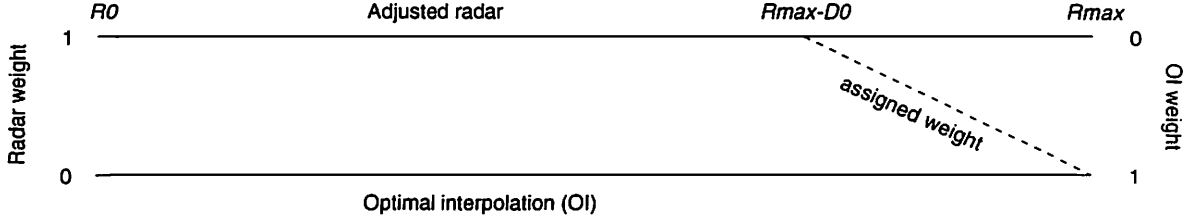


Figure 6.5: Concept for merging gauge adjusted radar with optimally interpolated gauge images according to distance. Distances range from R_0 to R_{max} , and the two images are linearly interpolated within the range $R_{max} - D_0$ to R_{max} , where D_0 is the decorrelation distance described in Section 6.5.

where r is the assigned correlation coefficient, d is the distance from an analysis pixel to a given observation, and D_0 is the analytically derived decorrelation distance presented in Section 6.5. In order to manage OI results for situations with very small scale precipitation patterns, which the observation density clearly cannot support, the value of D_0 has a lower bound of 40 km. This lower bound is only applied to the interpolation of gauge observations.

The resulting interpolated field ($OI_{(i,j)}$) is transformed to the high resolution RR image geometry specified in Table 6.1 using the Cressman weighting function (Equation 3.3) with an R value of 5.5 output grid pixels.

The strategy for merging of the gauge adjusted and OI images is illustrated in Figure 6.5. The distance composite and the spatial decorrelation distance, described in Section 6.5, are used to determine weights in a linear interpolation between the two images. The final product thus becomes

$$RR_{(i,j)} = \begin{cases} R_{r(i,j)}, & R_{(i,j)} \leq R_{max} - D_0 \\ w_{r(i,j)}R_{r(i,j)} + w_{oi(i,j)}OI_{(i,j)}, & R_{max} - D_0 < R_{(i,j)} < R_{max} \\ OI_{(i,j)}, & R_{(i,j)} \geq R_{max}. \end{cases} \quad (6.16)$$

where

$$w_{r(i,j)} = \frac{R_{(i,j)} - (R_{max} - D_0)}{D_0} \quad (6.17)$$

and $w_{oi(i,j)} = 1 - w_{r(i,j)}$. Values less than 0.1 mm in $RR_{(i,j)}$ are truncated to zero.

This strategy is simple and robust and it assumes that all radars have the same R_{max} . We know from Chapter 3 that most BALTRAD radars have an $R_{max} = 240$ km, so this value is used in the merging process. However, some radars have a different maximum ranges and this leads to artifacts in the final RR product, since the merging will not take place over the full range between $R_{max} - D_0$ and R_{max} . This can be clearly seen in the areas covered by the German and Polish radars in the complete RR product illustrated in Figure 6.6. Dealing with this more comprehensively is an area which requires more attention and should be the subject of future research.

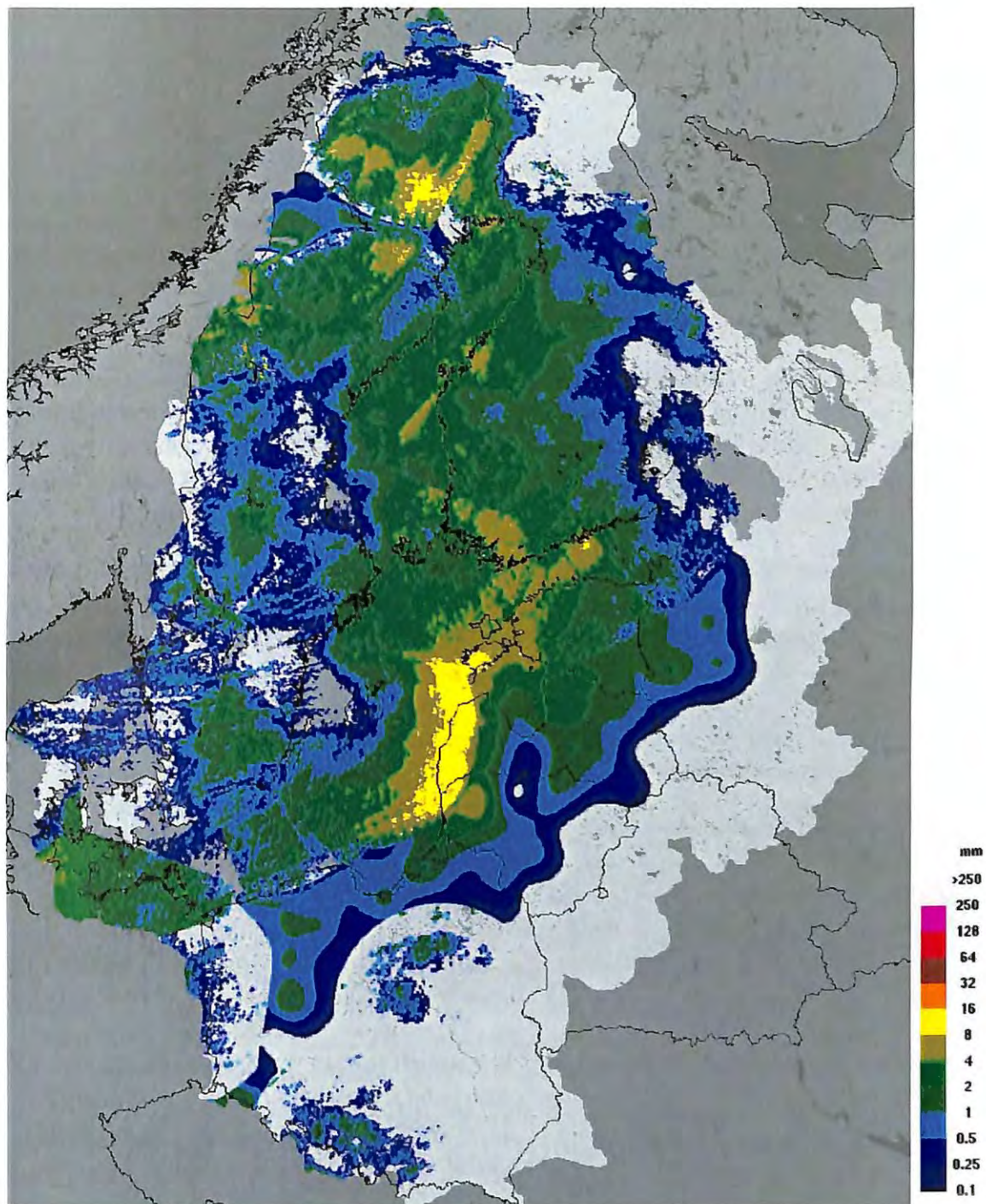


Figure 6.6: Merged gauge adjusted radar and optimal interpolation of corrected gauge sums. February 7, 2000, 18 UTC.

Table 6.3: *Biases and explained variances (r^2) when comparing logged independent gauge observations with logged unadjusted and adjusted radar sums. April 10-November 9, 1999. $n=2596$.*

Gauges vs.	Bias	r^2
Unadjusted radar	0.224	0.18
Adjusted radar	0.008	0.3

6.11 Validation

When generating the RR products, all of the radar and gauge observations are used in the analyses. However, during the BRIDGE Pilot Phase and the first few weeks of the BRIDGE Base-Line Period, a version of the RR product was produced continuously with the objective being to validate the method's performance.

The method of cross validation is an appropriate tool for this task. It is often conducted using a limited number of cases whereby around 10% of the observations are reserved for validation. The process is repeated until all observations have been used as independent data. The disadvantage of this approach is that it makes heavy use of computer resources, since the analysis must be continuously rerun.

An alternative approach, applied here, is to run a so-called continuous validation whereby 10% of the observations are excluded from each analysis once only. Instead of rerunning the same analysis, the same approach is applied over a long temporal series of analyses. This has been done for the period April 10 to November 9, 1999 for each 12-hour SYNOP term. It should be noted that the state of the analysis methods were not in their final form when these activities were conducted but that they were very similar to those presented in previous Sections of this Chapter.

The period ranged from early spring to late autumn and included a warm summer and autumn with a large proportion of small-scale convective precipitation events. This period also contained a significant number of events with severe anomalous propagation (AP). The methods used to treat AP echoes, presented in Section 4.4, were introduced in mid-June and were not applied to data previous to this point in time. Even with these methods applied, there were numerous cases where the final products remained contaminated with some AP echoes. Another issue which complicated matters was that the data from the Finnish radars were not subject to any Doppler signal processing during a period stretching from early June to mid-October, the result being manifested in the form of AP echoes and system noise. In summary, the period used for continuous validation contained complicated weather and propagation conditions, along with substandard data quality from several radars.

For each term, 10% of the gauge observations were saved, as were their corresponding radar sums both before and after gauge adjustment. The 10-logarithm of these values were taken as a way of approximating a normal sample distribution. Precipitation distributions otherwise tend to be skewed, which cannot be easily used when deriving descriptive statistics. Linear regressions were fitted between gauge values and unadjusted radar, and gauge values and adjusted radar. Biases between these

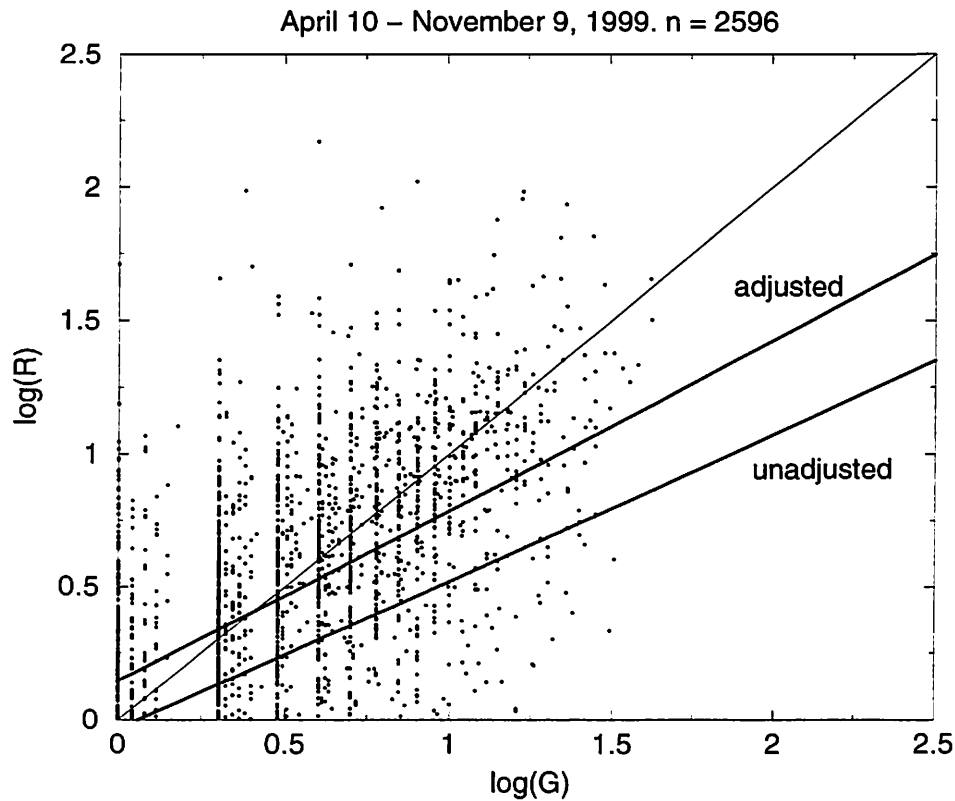


Figure 6.7: Scatterplot of gauge values against corresponding adjusted radar sums, along with fitted relations for both adjusted and unadjusted radar.

were calculated as were the explained variances. These results are provided in Table 6.3. The results are also illustrated in Figure 6.7.

The results in Table 6.3 indicate that the gauge adjustment technique succeeds in minimizing the bias between gauges and adjusted radar. While explained variances are low, that derived using adjusted radar is significantly higher than that found with unadjusted radar which reveals a more quantitatively useful product in the adjusted radar. When visualizing the results in Figure 6.7, the result is very noisy. The linear relations reveal that unadjusted radar levels are consistently lower than gauge levels. The higher Y-axis offset found with the relation using adjusted radar, along with a slightly steeper slope, show that adjustment leads to higher radar values with small accumulations and lower radar values with large accumulations. This can be attributed to sampling differences between gauge and radar arising from the small scale of the convective precipitation events; this leads to situations where radar observes precipitation which falls between gauges. Another contributing factor is the occurrence of AP echoes in radar which are not matched by gauge observations. Larger scale precipitation patterns and higher quality radar data may have resulted in better correspondence between gauges and radar.

A future research task should be to perform a systematic and comprehensive validation of the gauge adjustment technique presented in this Chapter. Validation should be conducted for differing precipitation types and the effect of adjustment on radar data's range dependency should be determined.

7 Vertical Wind and Reflectivity Profiles (WP)

This Chapter presents the wind profile (WP) product available at the BRDC, along with those institutes providing the product and the methods used to generate it.

Doppler weather radars are able to measure winds by comparing the phase of a pulse at reception with its phase at transmission. The wind velocity component which a radar measures is radial which means that it is the wind's speed relative to the radar's position. In other words, a wind blowing at a 90° angle to a radar will give a zero radial wind velocity. The methods for extracting wind information are more direct than those used to derive precipitation intensities, which arguably makes Doppler radars more useful for measuring winds. Radars have two fundamental limitations when used to measure winds:

- availability of radar targets, and
- limited unambiguous velocity due to radar hardware and signal processing.

The latter of these two issues has been recently addressed by Keeler et al. (1999) and will not be discussed further in this report.

Radial winds are measured and collected in polar volume format and can be used to derive vertical profiles of wind speed and direction. Several techniques have been developed over the years for this, a couple of which are presented or discussed in this Chapter. Radar winds are based on measurements of precipitation, but can also originate from insects, birds, aircraft, and sea waves. Andersson (1998) shows that profiles from Swedish radars are available more than 90% of the time from the planetary boundary layer during summer conditions, and that the availability is still over 80% on a more-or-less annual basis. Availabilities from upper levels were, however, lower. He also found radar winds to be compatible in accuracy to those from radiosonde measurements, the conclusion being that radar winds provide a viable compliment to those from radiosoundings.

7.1 DNMI

Vertical wind profiles are sent through NORDRAD using the BUFR code touched on in Section 2.9. The variables in these files are height, wind speed and wind direction. The unambiguous velocity interval is ± 48 m/s due to the staggered pulse repetition frequency (900 and 1200 Hz) of the Ericsson radar. Resolution in speed is 0.375 m/s in the original radial wind data.

The algorithm used to generate the WP from DNMI is the Andersson (1992b) Velocity Azimuth Display (VAD) method. The characteristics of this algorithm will be presented in more detail in Section 7.2, below.

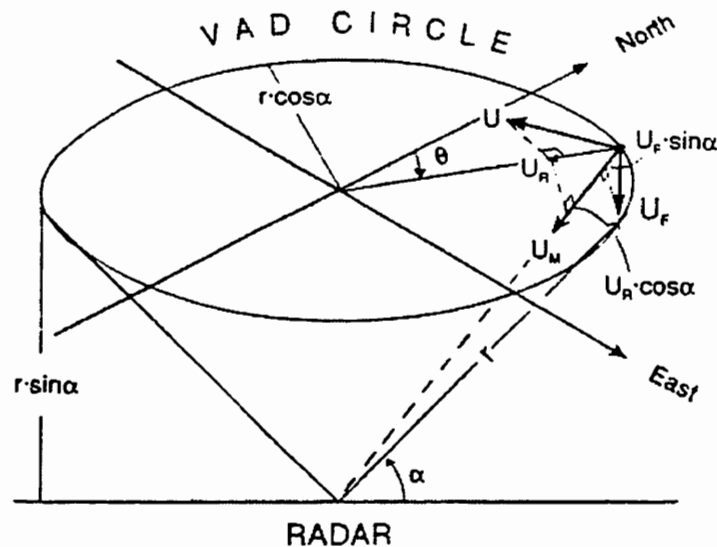


Figure 7.1: VAD circle and associated variables. From Andersson (1992b).

7.2 SMHI

Polar volume data of radial wind velocity and reflectivity factor are transferred from each radar node (except Radar Göteborg) to SMHI, Norrköping, where they are centrally processed at the BRDC.

The VAD algorithm developed by Andersson (1992b) has been modified slightly and rewritten. This version of the VAD algorithm is that used routinely at the BRDC. What follows is a presentation of this implementation. The VAD circle and schematics are presented in Figure 7.1.

It is important to insure that radar measurements of wind are of as high quality as possible. A simple way of doing so is to analyze data at relatively short ranges from the radar, thus minimizing accuracy problems associated with large pulse volumes. At the BRDC, this is accomplished by analyzing data out to a maximum slant range of 25 km. Within this range, all scans of data are evaluated, as are all azimuth gates and range bins contained in them.

For each scan, all possible slant range distances (≤ 25 km) are determined. At each range, the values from all azimuth gates are collected and these comprise the VAD circle for that scan and slant range. Whereas Andersson (1992b) interpolated the values in each circle to equidistant 10° locations around the circle, the BRDC's VAD algorithm leaves the values in their original form. The former strategy is designed to derive VAD circles with content as evenly spread as possible, thus making it possible to derive profiles from situations with few radar echoes. The latter strategy is designed to maximize the accuracy of the derived profile since no smoothing is carried out.

Each circle is divided into two 180° halves and pairs of values with 180° offsets are matched. Individual values with no matches are discarded and the matched point

pairs are summed. The only constraint is that a minimum of three summed values must be present before continuing.

If v is an array containing N matched point sums, then the average radial wind velocity (m/s) becomes

$$U_m = \frac{\sum_{i=1}^N v_i}{2N}. \quad (7.1)$$

Using the value of U_m , the north (a) and east (b) wind components are determined using a least squares fit. These wind components are valid at the radar and the wind's variation is assumed to be linear. For each VAD circle containing n radial wind velocity values (w) and matching azimuth gate angles (θ)

$$a = (\bar{C} - (SC \cdot \bar{S}/S^2))/(C^2 - (SC)^2/S^2) \quad (7.2)$$

and

$$b = (\bar{S} - a \cdot SC)/S^2 \quad (7.3)$$

where the temporary variables are

$$\bar{C} = \sum_{i=1}^n w_i - U_m \cos \theta_i \quad (7.4)$$

$$\bar{S} = \sum_{i=1}^n w_i - U_m \sin \theta_i \quad (7.5)$$

$$SC = \sum_{i=1}^n \sin \theta_i \cos \theta_i \quad (7.6)$$

$$C^2 = \sum_{i=1}^n \cos^2 \theta_i \quad (7.7)$$

and

$$S^2 = \sum_{i=1}^n \sin^2 \theta_i. \quad (7.8)$$

A quality control step is then performed in order to evaluate the integrity of the a and b wind components. The variance of the residuals to the modelled circle (σ^2) determined as

$$\sigma^2 = \sum_{i=1}^n (z_i - w_i)^2 / \sum z_i^2 \quad (7.9)$$

where the residual

$$z_i = U_{m_i} + (a \cdot \cos \theta_i) + (b \cdot \sin \theta_i). \quad (7.10)$$

Values of a and b are rejected where $\sigma^2 > 0.1$ and the given VAD circle is not subject to further analysis.

Accepted wind components are used to derive the direction of the wind vector

$$\psi = \arctan(a/b) \quad (7.11)$$

which, in turn, is used to derive the wind direction dd according to

$$dd = \begin{cases} 270 - \psi, & b > 0 \\ 90 - \psi, & b \leq 0. \end{cases} \quad (7.12)$$

The wind speed ff is given by

$$ff = \sqrt{a^2 + b^2} / \cos \alpha \quad (7.13)$$

where α is the antenna's elevation angle for the given scan. The height above sea level (h) of the given VAD circle is

$$h = H + \sin \alpha \cdot r \quad (7.14)$$

where H is the height of the radar's antenna and r is the slant range of the given VAD circle. This approach does not account for standard beam refraction and the maximum error it produces is approximately -36 m (or 12%) at the maximum slant range of 25 km and an elevation angle of 0.5° .

For each accepted VAD circle, its corresponding reflectivity factor (dBZ) value is calculated as the arithmetic average of all linearized, non-zero reflectivities in the circle. Additionally, the sample size is determined for each circle as the sum of all valid radial wind values. The latter variable is an important indirect indicator of the quality of a given set of values in the vertical profile.

When all possible circles have been evaluated, the resulting vertical profile is integrated vertically. This is done through the use of a predefined integration length of 200 m . Mean values and standard deviations of dd and ff are calculated; the mean height within each interval is also determined, as is the mean reflectivity factor value. The circle sample sizes are summed within each interval.

7.3 FMI

Wind profiles from FMI arrive at the BRDC through the regular internet in FMI's internal ASCII-based file format. These are converted to the common BALTRAD file format (Michelson 1999) and placed in the archive.

The algorithm used operationally by FMI to produce wind profiles is referred to as Volume Velocity Processing (VVP) and is presented in detail by Waldteufel and Corbin (1979). The implementation of this algorithm is found in software developed by SIGMET Inc. (SIGMET 1999).

The primary difference between VAD and VVP techniques is that, while VAD analyzes the data from an individual circle, VVP defines a narrow range of altitudes in the form of a cylinder and analyzes data from all scans which intersect the cylinder. FMI, for example, defines a set of 200 m thick volumes when deriving their VVP product. The VVP algorithm is more mathematically rigorous than VAD and, according to Waldteufel and Corbin (1979), offers the following advantages:

- High altitudes or elevation angles do not contaminate the calculations of mean horizontal velocity components, the horizontal divergence, and the vertical air velocity.
- A more direct estimate of the vertical component.
- Derivation of all three velocity components enables a control of the procedure's validity through comparison of successive cylinders.

Like all single-Doppler algorithms, VVP assumes a linear wind field. Similarly to VAD, VVP is sensitive to departures from linearity. If a nonlinearity has a scale which is larger than the analyzed volume, then the calculated vertical shear will contain errors. These types of problems can be reduced by defining volumes with small radii, much like use of a maximum range used with the VAD technique above. Another characteristic of the VVP technique is that the use of cylindrical volumes results in a low-pass filtering of the fine structure of the wind field, the consequence being that the resulting winds are more representative at the mesoscale. The equivalent effect does not take place using the VAD technique since the divergence is calculated exactly from a given circle (and may include contamination from the precipitation's vertical velocity).

In operational environments such as the BRDC, the VVP and VAD algorithms can be considered functionally equivalent. An objective comparison of the two using data from the BALTRAD network would be a valuable contribution to the understanding of methods used to derive wind profiles from weather radar data.

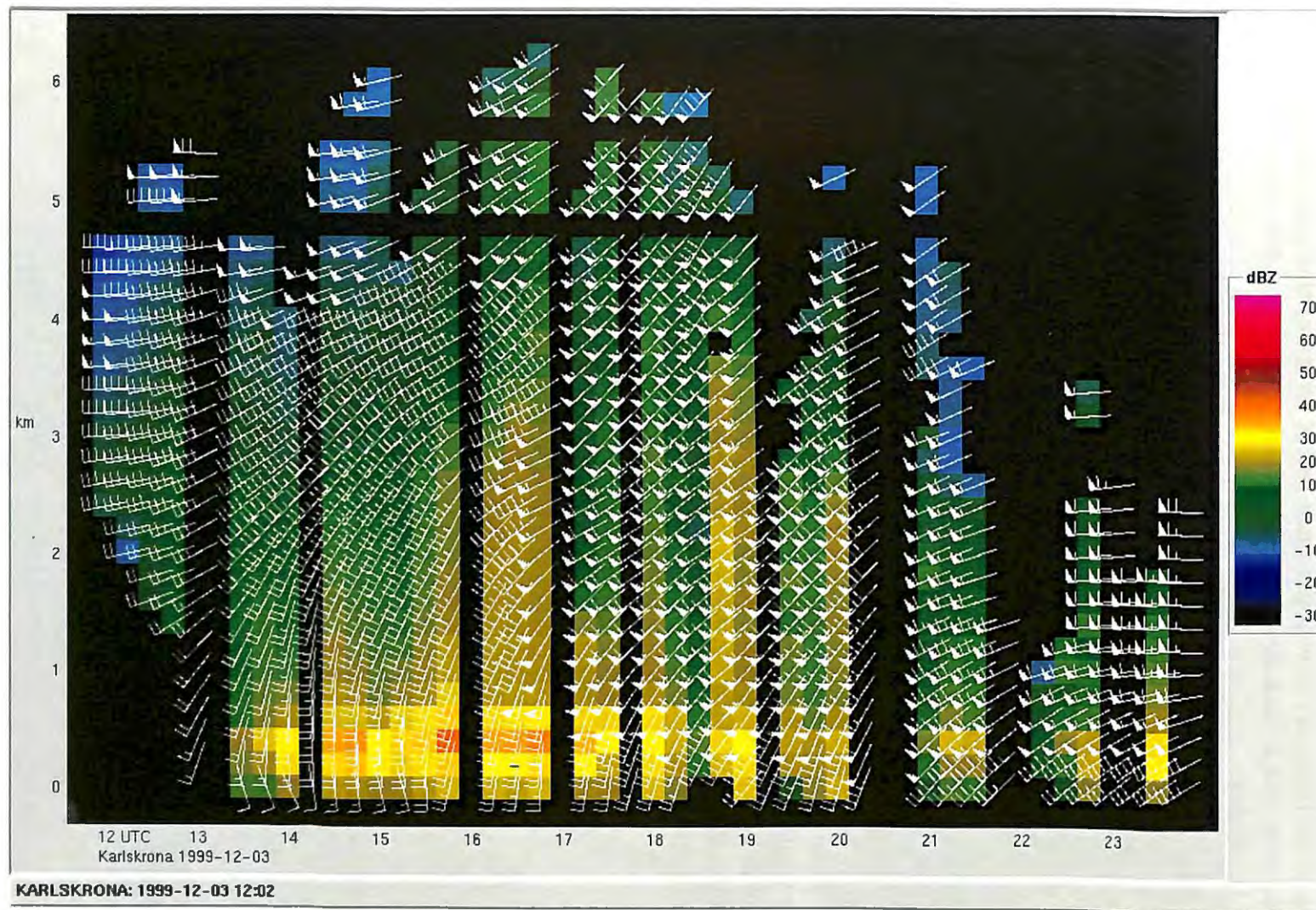
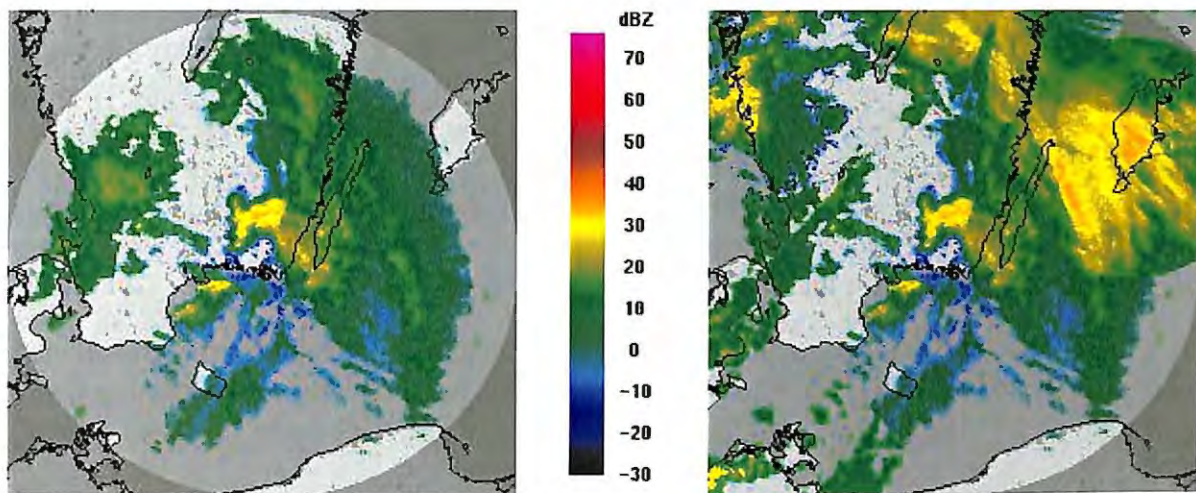


Figure 7.2: The December 3, 1999, storm over southern Scandinavia as seen through BALTRAD WP products from Radar Karlskrona.

7.4 Example

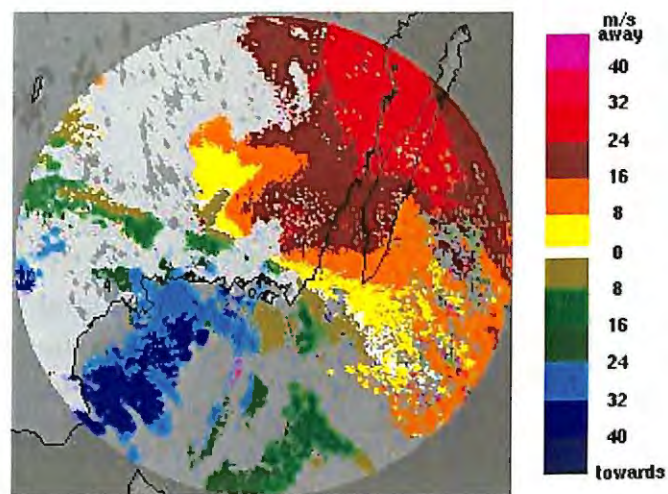
An example of a time-height plot of BALTRAD WP products is provided in Figure 7.2. On this day, December 3, 1999, a deep depression passed through southern Scandinavia. In Denmark it was the most severe storm of the 20th century. Radar Karlskrona provided a data series which was only broken in a few places during the course of the storm.

Surface winds shifted from south-south-easterly to south-westerly during the afternoon and into the evening, while upper-level winds were from the west to south-west throughout. The winds increased in strength following an area of frontal precipitation giving reflectivities upwards of 40 *dBZ*. Over 70 *kt* average wind speeds were observed at altitudes as low as around 800 *m a s l* during the evening. A hook echo can be discerned from reflectivities close to the radar in the DBZ product from 18:30 UTC (Figure 7.3a). The corresponding radial wind velocity PPI image (Figure 7.3c) helps reveal the presence of a local vortex in the wake of the frontal precipitation. The reflectivities from the vortex are very high and probably originate from wet snow in a melting layer; attenuation of the radar signal and beam overshooting are the likely explanations for the lack of precipitation echoes to the northwest, behind the vortex. Attenuation and partial beam overshooting may also account for relatively weak reflectivities from the frontal precipitation moving to the northeast over the Baltic Sea. The reflectivities from Radar Hemse for the same time were much higher, as can be seen in the subimage covering the same area from the DBZC product (Figure 7.3b).



(a) DBZ product.

(b) DBZC subimage.



(c) PPI of radial wind velocity.

Figure 7.3: The December 3, 1999, storm over southern Scandinavia as seen by Radar Karlskrona at 18:30 UTC. (Note the difference in maximum range between DBZ and radial wind velocity images.)

8 Summary

The Baltic Sea Experiment (BALTEX) is the European regional project within the Global Energy and Water Cycle Experiment (GEWEX), with contributions from 10 countries in the Baltic Sea's drainage basin. GEWEX has been launched by the World Meteorological Organization (WMO), the International Council of Scientific Union (ICSU) and the Intergovernmental Oceanographic Commission (IOC), as part of the World Climate Research Programme (WCRP). The BALTEX Working Group on Radar (WGR) is responsible for coordinating weather radar activities within the framework of BALTEX, including the establishment and operation of a Radar Data Centre (BRDC) which can provide BALTEX with wind and precipitation datasets. This report presents the state of the WGR and the BALTEX Radar Network (BALTRAD). Those products being generated at the BRDC are presented and discussed, as are the methods used to create them.

The BALTRAD network consists of 29, mostly C-band, radars in six countries. Communications to/from the BRDC are conducted both through operational lines and through provisional Internet-based solutions. The BRDC operates in near-real time.

The DBZ product is defined as "a 500 *m* Pseudo-CAPPI or the closest thing to it". Horizontal and temporal resolutions are 2 *km* and 15 minutes respectively, and the image depth is 8-bits. DBZ products are individual radar reflectivity factor (*dBZ*) images which are transformed to a common projection and subjected to simple quality control procedures such that they may be used to generate higher level products.

The DBZC product is a composite image for the BALTRAD coverage area containing radar reflectivity factor (*dBZ*) and which is generated every 15 minutes with a horizontal resolution of 2 *km*. It makes use of individual DBZ products. A compositing algorithm which makes use of a high resolution digital elevation model is presented and discussed. Quality control is conducted using the difference between Meteosat-b IR brightness temperatures and analyzed 2-m temperatures; areas not containing potentially precipitating clouds are identified with this method and radar echoes in them are deemed spurious and removed.

A systematic correction of 12-hourly gauge observations from the real-time synoptical network is conducted which makes use of a statistical method developed for use with gauge types commonly available in the BALTEX Region. This method makes use of spatially analyzed variables with a temporal resolution of one hour. The largest correction is for the flow distortion error caused by wind, but the method takes into account temperature, precipitation intensity, wetting loss, and evaporation loss. Corrected gauge data are not a BRDC product.

The RR product is a gauge adjusted three and 12-hourly radar-based accumulated precipitation image which makes use of DBZ products and corrected gauge observations. The gauge adjustment technique is based on the gauge-to-radar ratio. A distance-dependent adjustment factor is derived and this is combined with a spa-

tially analyzed adjustment factor according to the observation density and estimated spatial decorrelation distance. The final adjustment field applied to radar accumulations is shown to minimize the bias between radar and gauge sums while raising the explained variance, compared to unadjusted radar sums. Areas not covered by radar are subjected to an optimal interpolation of corrected gauge sums, and this field is merged with the gauge adjusted radar field in order to cover the entire BALTEX Region.

The WP product contains vertical profiles of wind speed, wind direction, reflectivity factor, and other associated variables, with a temporal resolution of 15 minutes and a vertical resolution of 200 *m*. The two methods used are the Velocity Azimuth Display technique (VAD) and the Velocity Volume Processing (VVP) technique, which are both presented and discussed.

9 Acknowledgements

Zdzisław Dziwit and Stanisław Moszkowicz of the Institute of Meteorology and Water Management in Legionowo, Poland, are gratefully acknowledged for their continuing efforts to manually supply the BRDC with data.

Tony Bakker of the European Centre for Medium Range Weather Forecasting in Reading, England, is gratefully acknowledged for helping establish ETR services between SMHI and our colleagues elsewhere.

Klaus-Jürgen Schreiber and Ilona Glaser of the German Weather Service in Offenbach are gratefully acknowledged for their efforts to set up the well-working data exchange through the ECMWF's ETR service.

Thomas Skogberg of the Finnish Meteorological Institute is gratefully acknowledged for his help in establishing well-working communications between FMI and the BRDC.

Paul Jacobsson of SMHI is gratefully acknowledged for managing the BRDC computer platform and archive.

Rickard Svensson, Anders Brodin and Arne Törnvall, all formerly of SMHI, are thanked for their assistance in establishing network communications between SMHI and institutes contributing data to the BRDC.

Finally, Hans-Jörg Isemer, the former Secretary of the BALTEX Secretariat, is happily acknowledged for asking provocative questions at strategic moments. Doing so has sparked the BALTEX Working Group on Radar's commitment which has led to the establishment of the BRDC and its contributions to BALTEX.

The development of the BALTEX Radar Data Centre and its software, including the product algorithms, has been conducted within the framework of two projects. The first is the "Pilot Study of Evaporation and Precipitation in the Baltic Sea - PEP in BALTEX" funded by the European Commission under contract ENV4-CT97-0484 and by the Swedish Environmental Protection Agency. The second project is an internal SMHI project simply called "BALTEX Radar Data Centre". Both sources of funding are gratefully acknowledged.

10 List of Acronyms

AP	Anomalous Propagation
BALTEX	Baltic Sea Experiment
BALTRAD	BALTEX Weather Radar Network
BRDC	BALTEX Radar Data Centre
BRIDGE	BALTEX Main Experiment
BUFR	Binary Universal Form for the Representation of Meteorological Data
CAPPI	Constant Altitude Plan Position Indicator
CERAD	Central European Radar Network
DCM	Dynamic Correction Model
DEM	Digital Elevation Model
DMI	Danish Meteorological Institute
DNMI	The Norwegian Meteorological Institute
DWD	German Weather Service
ECMWF	European Centre for Medium Range Weather Forecasting
EMHI	Estonian Meteorological and Hydrological Institute
ETR	Electronic Transfer Routing
EWIS	Ericsson Weather Radar Information System
FMI	Finnish Meteorological Institute
GEWEX	Global Energy and Water Cycle Experiment
GMS	Geostationary Meteorological Satellite
GTS	Global Telecommunications System
HIRLAM	High Resolution Limited Area Model
ICSU	International Council of Scientific Union
IOC	Intergovernmental Oceanographic Commission
IMGW	Institute of Meteorology and Water Management
LHA	Latvian Hydrometeorological Agency
LUT	Lookup Table
m a s l	Mean altitude above sea level
MDE	Minimum Distance to Earth
MESAN	Mesoscale Analysis System
METEOSAT	Geostationary Meteorological Satellite
NORDRAD	Nordic Weather Radar Network
OPERA	Operational Programme for the Exchange of Weather Radar Information
PPI	Plan Position Indicator
RMDCN	Regional Meteorological Data Communication Network
SMHI	Swedish Meteorological and Hydrological Institute
SWERAD	Swedish Radar Network
SYNOP	Synoptical Weather Station Network
USGS	United States Geological Survey
VAD	Velocity Azimuth Display

continued on next page

continued from previous page

VVP	Velocity Volume Processing
WCRP	World Climate Research Programme
WGR	BALTEX Working Group on Radar
WMO	World Meteorological Organization

11 References

- Alberoni, P. P., Andersson, T., Mezzasalma, P., Michelson, D. B., and Nanni, S., 2000. Use of the vertical reflectivity profile for identification of anomalous propagation. *Met. Apps.* (accepted for publication).
- Andersson, T., 1992a. Image Mosaics from Swedish Weather Radars. In Collier, C. G. (Ed.), *COST 73 International Weather Radar Networking. Final Seminar of the COST Project 73*, pp. 139–142. Brussels: European Commission. EUR 13649 EN. 332 pp.
- Andersson, T., 1992b. A method for estimating the wind profile and vertical speed of targets from a single Doppler radar. In *Instruments and Observing Methods, Rep. No. 49*, WMO/TD No. 462, pp. 380–386.
- Andersson, T., 1998. VAD winds from C band Ericsson Doppler Weather Radars. *Meteorol. Zeitschrift* 7, 309–319.
- BALTEX, 1995. Baltic Sea Experiment BALTEX - Initial Implementation Plan. Publication No. 2, International BALTEX Secretariat, GKSS Research Center, Geesthacht.
- Barbosa, S., 1994. Brief Review of Radar-Raingauge Adjustment Techniques. In Almeida-Teixeira, M. E., Fantechi, R., Moore, R., and Silva, V. M. (Eds.), *Advances in radar hydrology*, pp. 148–169. Brussels: European Commission. EUR 14334 EN.
- Barnes, S. L., 1964. A technique for maximizing details in numerical weather map analysis. *J. Appl. Meteor.* 3, 396–409.
- Barnes, S. L., 1973. Mesoscale Objective Map Analysis Using Weighted Time-Series Observations. Technical Report NOAA Technical Memorandum ERL NSSL-62, National Severe Storms Laboratory, Norman, Oklahoma. 60 pp.
- Brandes, E. A., 1975. Optimizing Rainfall Estimates with the Aid of Radar. *J. Appl. Meteor.* 14, 1339–1345.
- Brandt, R., Collier, C., Isemer, H.-I., Koistinen, J., Macpherson, B., Michelson, D., Overgaard, S., Raschke, E., and Svensson, J., 1996. BALTEX Radar Research - A Plan for Future Action. Publication No. 6, International BALTEX Secretariat, GKSS Research Center, Geesthacht, Germany.
- Browning, K. A., 1990. Rain, rainclouds and climate. *Quart. J.R. Met. Soc.* 116(495), 1025–1051.
- Brussaard, G. and Watson, P. A., 1995. *Atmospheric modelling and millimetre wave propagation*. Chapman and Hall.
- Carlsson, I., 1995. NORDRAD - Weather Radar Network. See Collier (1995), pp. 45–52. EUR 16013 EN. 814 pp.
- Collier, C. G. (Ed.), 1995. *COST 75 Weather Radar Systems*. Brussels: European Commission. EUR 16013 EN. 814 pp.
- Collier, C. G., 1996. *Applications of Weather Radar Systems. A guide to uses of radar data in meteorology and hydrology* (2 ed.). Chichester/London: Praxis/John Wiley and Sons.

- Cressman, G. W., 1959. An operational objective analysis system. *Mon. Wea. Rev.* 87, 367–374.
- Dahlberg, L., 1996. Analysis of hardware and software differences in the NOR-DRAD Weather Radars and how these will affect calibration and measurements of the dBZ-values. Consultant's report, RadMet AB. Rev. B. 29 pp.
- Daley, R., 1991. *Atmospheric Data Analysis*. New York: Cambridge University Press. 457 pp.
- Ebert, E. E. and Weymouth, G. T., 1999. Incorporating Satellite Observations of "No Rain" in an Australian Daily Rainfall Analysis. *J. Appl. Meteor.* 38, 44–56.
- Evenden, G. I., 1995. *Cartographic Projection Procedures for the UNIX Environment-A User's Manual*. U.S. Geological Survey, Coastal and Marine Geology Program, 384 Woods Hole Rd., Woods Hole, MA 02543, USA. 64 pp.
- Førland, E. J., Allerup, P., Dahlström, B., Elomaa, E., Jónsson, T., Madsen, H., Perälä, J., Rissanen, P., Vedin, H., and Vejen, F., 1996. Manual for operational correction of Nordic precipitation data. Report nr. 24/96, DNMI, P.O. Box 43, Blindern, Oslo, Norway. 66 pp.
- Graham, L. P., 2000. *Large-Scale Hydrologic Modeling in the Baltic Basin*. Ph. D. thesis, Dept. Civil and Environmental Engineering, Royal Institute of Technology, SE-100 44 Stockholm, Sweden. ISSN 1400-1284.
- Häggmark, L., Ivarsson, K. I., and Olofsson, P. O., 1997. MESAN - Mesoskalig Analys. RMK 75, SMHI, S-601 76 Norrköping, Sweden. 77 pp. (in Swedish).
- Henja, A. and Michelson, D. B., 1999. Improved polar to cartesian radar data transformation. In *Preprints AMS 29th Int. Conf. on Radar Met.*, pp. 252–255. AMS.
- IMGW, 1999. The Hydrological and Meteorological Monitoring Forecasting and Protection System. Flood management and hazard reduction. Emergency Flood Recovery Project, financed by the World Bank. Publishing Institute, Warsaw. 70 pp.
- Källén, E., 1996. HIRLAM Documentation Manual, system 2.5. Technical report, SMHI, S-601 76 Norrköping, Sweden.
- Karlsson, K.-G., 1996. Cloud classifications with the SCANDIA model. RMK 67, SMHI, S-601 76 Norrköping, Sweden. 36 pp.
- Keeler, R. J., Zrnica, D. S., and Frush, C. L., 1999. Review of Range Velocity Ambiguity Mitigation Techniques. In *Preprints AMS 29th Int. Conf. on Radar Met.*, pp. 158–163. AMS.
- Kerr, D. E. (Ed.), 1951. *Propagation of Short Radio Waves*. New York: Dover Publications. 728 pp.
- Koistinen, J., King, R., Saltikoff, E., and Harju, A., 1999. Monitoring and assessment of systematic measurement errors in the NORDRAD network. In *Preprints AMS 29th Int. Conf. on Radar Met.*, pp. 765–768. AMS.

- Koistinen, J. and Michelson, D. B., 1997. Weather Radar Research for the Baltic Sea Experiment: BALTRAD. In *Preprints 28th Conf. on Radar Met.*, pp. 190–191. AMS.
- Koistinen, J. and Puhakka, T., 1981. An improved spatial gauge-radar adjustment technique. In *Proc. 20th Conf. on Radar Met.*, pp. 179–186. AMS.
- Marshall, J. S. and Palmer, M. K., 1948. The distribution of raindrops with size. *J. Meteor.* 5, 165–166.
- Michelson, D. B., 1999. RAVE User's Guide. SMHI, SE-601 76 Norrköping, Sweden. 51 pp.
- Michelson, D. B., Andersson, T., Collier, C. G., Dziewit, Z., Koistinen, J., Overgaard, S., Riedl, J., and Zhukov, V., 1999. The International Radar Network for the Baltic Sea Experiment. In *Preprints 29th AMS Int. Conf. on Radar Met.*, pp. 317–320. AMS.
- Moszkowicz, S., 1995. Algorithms for Meteorological Phenomena Recognition and AP Echoes Suppression on Automated Weather Radar System AMSR. See Collier (1995), pp. 239–248. EUR 16013 EN. 814 pp.
- Omstedt, A., Meuller, L., and Nyberg, L., 1997. Interannual, seasonal and regional variations of precipitation and evaporation over the Baltic Sea. *Ambio* 26(8), 484–492.
- OPERA, 1999. URL: <http://www.chmi.cz/OPERA/>.
- Randeu, W. L., Köck, K. F., and Leitner, T., 1996. Realisation of the Central European Weather Radar Network (CERAD). Final Report - Draft, ICWP Technical University of Graz. 37 pp.
- Richardus, P. and Adler, R., 1972. *Map Projections*. Amsterdam: North-Holland Publishing Co. 174 pp.
- Rubel, F., 1996. PIDCAP - Quick Look Precipitation Atlas. *Österreichisches Beiträge zu Meteorologie und Geophysik* (15). 95 pp.
- Rubel, F. and Hantel, M., 1999. Correction of Daily Rain Gauge Measurements in the Baltic Sea Drainage Basin. *Nordic Hydrology* 30(3), 191–208.
- Rubel, R., 1998. PIDCAP Ground Truth Atlas. *Österreichisches Beiträge zu Meteorologie und Geophysi* (18). 76 pp.
- Rutgersson, A., Bumke, K., Clemens, M., Foltescu, V., Michelson, D., and Omstedt, A., 2000. Precipitation estimates over the Baltic Sea: present state of the art. *Nordic Hydrology*. (submitted).
- Schreiber, K. J., 1998. Der Radarverbund des Deutschen Wetterdienstes. *Annalen der Meteorologie* 38, 47–64. DWD, Offenbach. (in German).
- SIGMET, 1999. IRIS/Open User's Manual. Woodland Park, 2 Park Drive, Suite 1. Westford, Mass. 01886, USA.
- Stensrud, D. J. and Fritsch, J. M., 1994. Mesoscale convective systems in weakly forced large-scale environments. Part III Numerical simulations and implications for operational forecasting. *Mon. Wea. Rev.* 122, 2084–2104.

- USGS, 1999. Global 30 Arc Second Elevation Data Set, EROS Data Center, Sioux Falls, SD. URL: <http://edcwww.cr.usgs.gov/landdaac/gtopo30/gtopo30.html>.
- VCS, 1995. VCS Nachrichtentechnik GmbH. Borgmannstraße 2, DE-44894 Boschum, Germany.
- Waldteufel, P. and Corbin, H., 1979. On the Analysis of Single-Doppler Radar Data. *J. Appl. Meteor.* 18, 532–542.
- Watson, R. J., 1996. *Data Comparisons for Spatially Separated Meteorological Radars*. Ph. D. thesis, Dept. Electronic Systems Engineering, University of Essex, UK. 284 pp.
- WMO, 1994. Report of the Working Committee on item 7.7 and 13. CIMO-XI, Geneva.

SMHI's publications

SMHI publishes six report series. Three of these, the R-series, are intended for international readers and are in most cases written in English. For the others the Swedish language is used.

Names of the Series	Published since
RMK (Report Meteorology and Climatology)	1974
RH (Report Hydrology)	1990
RO (Report Oceanography)	1986
METEOROLOGI	1985
HYDROLOGI	1985
OCEANOGRAFI	1985

Earlier issues published in serie RMK

- | | |
|---|--|
| <p>1 Thompson, T., Udin, I., and Omstedt, A. (1974)
Sea surface temperatures in waters surrounding Sweden.</p> <p>2 Bodin, S. (1974)
Development on an unsteady atmospheric boundary layer model.</p> <p>3 Moen, L. (1975)
A multi-level quasi-geostrophic model for short range weather predictions.</p> <p>4 Holmström, I. (1976)
Optimization of atmospheric models.</p> <p>5 Collins, W.G. (1976)
A parameterization model for calculation of vertical fluxes of momentum due to terrain induced gravity waves.</p> <p>6 Nyberg, A. (1976)
On transport of sulphur over the North Atlantic.</p> <p>7 Lundqvist, J.-E., and Udin, I. (1977)
Ice accretion on ships with special emphasis on Baltic conditions.</p> | <p>8 Eriksson, B. (1977)
Den dagliga och årliga variationen av temperatur, fuktighet och vindhastighet vid några orter i Sverige.</p> <p>9 Holmström, I., and Stokes, J. (1978)
Statistical forecasting of sea level changes in the Baltic.</p> <p>10 Omstedt, A., and Sahlberg, J. (1978)
Some results from a joint Swedish-Finnish sea ice experiment, March, 1977.</p> <p>11 Haag, T. (1978)
Byggnadsindustrins väderberoende, seminarieuppsats i företagsekonomi, B-nivå.</p> <p>12 Eriksson, B. (1978)
Vegetationsperioden i Sverige beräknad från temperaturobservationer.</p> <p>13 Bodin, S. (1979)
En numerisk prognosmodell för det atmosfäriska gränsskiktet, grundad på den turbulenta energiekvationen.</p> <p>14 Eriksson, B. (1979)
Temperaturfluktuationer under senaste 100 åren.</p> |
|---|--|

- 15 Udin, I., och Mattisson, I. (1979)
Havsis- och snöinformation ur datorbear-
betade satellitdata - en modellstudie.
- 16 Eriksson, B. (1979)
Statistisk analys av nederbördsdata. Del I.
Arealnederbörd.
- 17 Eriksson, B. (1980)
Statistisk analys av nederbördsdata. Del II.
Frekvensanalys av månadsnederbörd.
- 18 Eriksson, B. (1980)
Årsmedelvärden (1931-60) av nederbörd, av-
dunstning och avrinning.
- 19 Omstedt, A. (1980)
A sensitivity analysis of steady, free floating
ice.
- 20 Persson, C., och Omstedt, G. (1980)
En modell för beräkning av luftföroreningars
spridning och deposition på mesoskala.
- 21 Jansson, D. (1980)
Studier av temperaturinversioner och vertikal
vindskjuvning vid Sundsvall-Härnösands
flygplats.
- 22 Sahlberg, J., and Törnevik, H. (1980)
A study of large scale cooling in the Bay of
Bothnia.
- 23 Ericson, K., and Hårsmar, P.-O. (1980)
Boundary layer measurements at Klock-rike.
Oct. 1977.
- 24 Bringfelt, B. (1980)
A comparison of forest evapotranspiration
determined by some independent methods.
- 25 Bodin, S., and Fredriksson, U. (1980)
Uncertainty in wind forecasting for wind po-
wer networks.
- 26 Eriksson, B. (1980)
Graddagsstatistik för Sverige.
- 27 Eriksson, B. (1981)
Statistisk analys av nederbördsdata. Del III.
200-åriga nederbördsserier.
- 28 Eriksson, B. (1981)
Den "potentiella" evapotranspirationen i
Sverige.
- 29 Pershagen, H. (1981)
Maximisnödjun i Sverige (perioden
1905-70).
- 30 Lönnqvist, O. (1981)
Nederbördsstatistik med praktiska tillämp-
ningar.
(Precipitation statistics with practical appli-
cations.)
- 31 Melgarejo, J.W. (1981)
Similarity theory and resistance laws for the
atmospheric boundary layer.
- 32 Liljas, E. (1981)
Analys av moln och nederbörd genom
automatisk klassning av AVHRR-data.
- 33 Ericson, K. (1982)
Atmospheric boundary layer field experiment
in Sweden 1980, GOTEX II, part I.
- 34 Schoeffler, P. (1982)
Dissipation, dispersion and stability of
numerical schemes for advection and dif-
fusion.
- 35 Undén, P. (1982)
The Swedish Limited Area Model. Part A.
Formulation.
- 36 Bringfelt, B. (1982)
A forest evapotranspiration model using sy-
noptic data.
- 37 Omstedt, G. (1982)
Spridning av luftförorening från skorsten i
konvektiva gränsskikt.
- 38 Törnevik, H. (1982)
An aerobiological model for operational
forecasts of pollen concentration in the air.
- 39 Eriksson, B. (1982)
Data rörande Sveriges temperaturklimat.
- 40 Omstedt, G. (1984)
An operational air pollution model using
routine meteorological data.
- 41 Persson, C., and Funkquist, L. (1984)
Local scale plume model for nitrogen
oxides. Model description.

- 42 Gollvik, S. (1984)
Estimation of orographic precipitation by dynamical interpretation of synoptic model data.
- 43 Lönnqvist, O. (1984)
Congression - A fast regression technique with a great number of functions of all predictors.
- 44 Laurin, S. (1984)
Population exposure to SO and NO_x from different sources in Stockholm.
- 45 Svensson, J. (1985)
Remote sensing of atmospheric temperature profiles by TIROS Operational Vertical Sounder.
- 46 Eriksson, B. (1986)
Nederbörds- och humiditetsklimat i Sverige under vegetationsperioden.
- 47 Taesler, R. (1986)
Köldperioden av olika längd och förekomst.
- 48 Wu Zengmao (1986)
Numerical study of lake-land breeze over Lake Vättern, Sweden.
- 49 Wu Zengmao (1986)
Numerical analysis of initialization procedure in a two-dimensional lake breeze model.
- 50 Persson, C. (1986)
Local scale plume model for nitrogen oxides. Verification.
- 51 Melgarejo, J.W. (1986)
An analytical model of the boundary layer above sloping terrain with an application to observations in Antarctica.
- 52 Bringfelt, B. (1986)
Test of a forest evapotranspiration model.
- 53 Josefsson, W. (1986)
Solar ultraviolet radiation in Sweden.
- 54 Dahlström, B. (1986)
Determination of areal precipitation for the Baltic Sea.
- 55 Persson, C. (SMHI), Rodhe, H. (MISU), De Geer, L.-E. (FOA) (1986)
The Chernobyl accident - A meteorological analysis of how radionuclides reached Sweden.
- 56 Persson, C., Robertson, L. (SMHI), Grennfelt, P., Kindbom, K., Lövblad, G., och Svanberg, P.-A. (IVL) (1987)
Luftföroreningsepisoden över södra Sverige 2 - 4 februari 1987.
- 57 Omstedt, G. (1988)
An operational air pollution model.
- 58 Alexandersson, H., Eriksson, B. (1989)
Climate fluctuations in Sweden 1860 - 1987.
- 59 Eriksson, B. (1989)
Snödjupsförhållanden i Sverige - Säsongerna 1950/51 - 1979/80.
- 60 Omstedt, G., Szegö, J. (1990)
Människors exponering för luftföroreningar.
- 61 Mueller, L., Robertson, L., Andersson, E., Gustafsson, N. (1990)
Meso-γ scale objective analysis of near surface temperature, humidity and wind, and its application in air pollution modelling.
- 62 Andersson, T., Mattisson, I. (1991)
A field test of thermometer screens.
- 63 Alexandersson, H., Gollvik, S., Mueller, L. (1991)
An energy balance model for prediction of surface temperatures.
- 64 Alexandersson, H., Dahlström, B. (1992)
Future climate in the Nordic region - survey and synthesis for the next century.
- 65 Persson, C., Langner, J., Robertson, L. (1994)
Regional spridningsmodell för Göteborgs och Bohus, Hallands och Älvsborgs län. (A mesoscale air pollution dispersion model for the Swedish west-coast region. In Swedish with captions also in English.)
- 66 Karlsson, K.-G. (1994)
Satellite-estimated cloudiness from NOAA AVHRR data in the Nordic area during 1993.

- 67 Karlsson, K-G. (1996)
Cloud classifications with the SCANDIA model.
- 68 Persson, C., Ullerstig, A. (1996)
Model calculations of dispersion of lindane over Europe. Pilot study with comparisons to measurements around the Baltic Sea and the Kattegat.
- 69 Langner, J., Persson, C., Robertson, L., and Ullerstig, A. (1996)
Air pollution Assessment Study Using the MATCH Modelling System. Application to sulfur and nitrogen compounds over Sweden 1994.
- 70 Robertson, L., Langner, J., Engardt, M. (1996)
MATCH - Meso-scale Atmospheric Transport and Chemistry modelling system.
- 71 Josefsson, W. (1996)
Five years of solar UV-radiation monitoring in Sweden.
- 72 Persson, C., Ullerstig, A., Robertson, L., Kindbom, K., Sjöberg, K. (1996)
The Swedish Precipitation Chemistry Network. Studies in network design using the MATCH modelling system and statistical methods.
- 73 Robertson, L. (1996)
Modelling of anthropogenic sulfur deposition to the African and South American continents.
- 74 Josefsson, W. (1996)
Solar UV-radiation monitoring 1996.
- 75 Häggmark, L., Ivarsson, K.-I. (SMHI), Olofsson, P.-O. (Militära väderstjänsten). (1997)
MESAN - Mesoskalig analys.
- 76 Bringfelt, B., Backström, H., Kindell, S., Omstedt, G., Persson, C., Ullerstig, A. (1997)
Calculations of PM-10 concentrations in Swedish cities- Modelling of inhalable particles
- 77 Gollvik, S. (1997)
The Telelood project, estimation of precipitation over drainage basins.
- 78 Persson, C., Ullerstig, A. (1997)
Regional luftmiljöanalys för Västmanlands län baserad på MATCH modell-beräkningar och mätdata - Analys av 1994 års data
- 79 Josefsson, W., Karlsson, J.-E. (1997)
Measurements of total ozone 1994-1996.
- 80 Rummukainen, M. (1997)
Methods for statistical downscaling of GCM simulations.
- 81 Persson, T. (1997)
Solar irradiance modelling using satellite retrieved cloudiness - A pilot study
- 82 Langner, J., Bergström, R. (SMHI) and Pleijel, K. (IVL) (1998)
European scale modelling of sulfur, oxidized nitrogen and photochemical oxidants. Model development and evaluation for the 1994 growing season.
- 83 Rummukainen, M., Räisänen, J., Ullerstig, A., Bringfelt, B., Hansson, U., Graham, P., Willén, U. (1998)
RCA - Rossby Centre regional Atmospheric climate model: model description and results from the first multi-year simulation.
- 84 Räisänen, J., Döscher, R. (1998)
Simulation of present-day climate in Northern Europe in the HadCM2 OAGCM.
- 85 Räisänen, J., Rummukainen, M., Ullerstig, A., Bringfelt, B., Ulf Hansson, U., Willén, U. (1999)
The First Rossby Centre Regional Climate Scenario - Dynamical Downscaling of CO₂-induced Climate Change in the HadCM2 GCM.
- 86 Rummukainen, Markku. (1999)
On the Climate Change debate
- 87 Räisänen, Jouni (2000)
CO₂-induced climate change in northern Europe: comparison of 12 CMIP2 experiments.
- 88 Engardt, Magnuz (2000)
Sulphur simulations for East Asia using the MATCH model with meteorological data from ECMWF.

- 89 Persson, Thomas (2000)
Measurements of Solar Radiation in Sweden
1983-1998



Swedish Meteorological and Hydrological Institute
SE 601 76 Norrköping, Sweden.
Tel +46 11-15 80 00. Fax +46 11-17 02 07